Destabilization of bentonite interlayers by ultrasonication and pH control

A.A.A. Fauzi[1,2], A.F. Osman[1,2,*], M.A.A. Abdullah[2]

[1)] School of Materials Engineering, Universiti Malaysia Perlis, 02600 Arau, Perlis, Malaysia
[2)] School of Fundamental Science, Universiti Malaysia Terengganu, 21030 Kuala Terengganu, Terengganu, Malaysia

[*]Corresponding e-mail: azlin@unimap.edu.my

Keywords: Bentonite; destabilization; pH control; nitric acid

ABSTRACT – Destabilization process of natural Bentonite interlayers was done by ultrasonication and pH control in order to obtain loosely packed tactoids. The suspension of the ultrasonicated Bentonite was subjected to different pH conditions (pH 4, 5 and 6) prior to drying and testing. The Bentonite particle characteristics such as interlayer spacing and morphology were compared between the pristine and the destabilized Bentonites using FESEM and XRD. FESEM images revealed more loosely packed tactoids in the destabilized Bentonite as compared to its pristine counterpart. Greater platelet spacing and porosity can be observed in between the silicate platelets. However, XRD results indicated that basal spacings were not significantly changes upon the destabilization process.

1. INTRODUCTION

Bentonite is natural occurring clay composed of Montmorillonite and derived from deposited weathering volcanic ash [1]. It belongs to expandable 2:1 phyllosilicate smectite clay family in which octahedral sheet is being sandwiched by two tetrahedral sheets. Tetrahedral sheet consists of silicon that are being surrounded by four oxygen atom. Octahedral sheet consists of aluminium that is surrounded by eight oxygen atom. They are held together by sharing oxygen atom. Bentonite are often used in polymer composite as filler because it is easily obtained and cheap. However, bentonite has close packed tactoid that can prevent polymer intercalation between the clay interlayers. Therefore, clay is commonly modified via cation exchange method to expand the interlayer spacing and subsequently facilitate polymer chain intercalation. However, this surface modification method has some drawbacks such as the high cost of the organic surfactant and its tendency to degrade upon high temperature melt compounding process [2]. In this work, an alternative method; the so called 'destabilization process' of Bentonite by ultrasonication and acid treatment was applied. Bentonite has pH dependant charges on the edge of the clay and permanent charge on the clay surface. The edge sited of clay is positive at low pH and the changes in the pH will influence the cohesive strength between the silicate interlayer, thereby the stability of tactoid formed [3, 4]. The closely packed tactoids can be opened up as the negative surface charge interacts with positive edge charge. Consequently, loosely packed clay tactoids can be obtained to allow better platelet exfoliation and dispersion within the polymer matrix. In this project, well dispersed and exfoliated bentonite filler was targeted to produce an optimize polymer/bentonite composite system.

2. METHODOLOGY

2.1 Materials

Ca-bentonite was obtained from Multifilla (M) Sdn. Bhd., 65% of Nitric Acid from Merck and dispersing medium used was deionized water.

2.2 Sample preparation

20g of Bentonite was weighed and dispersed in 100ml of deionized water. Then, the suspension was stirred for 15 minutes by ultrasonic probe. In the meantime, nitric acid was added to the solution by using dropper until it reaches pH4. Then, the mixture was further stirred for about 5 minutes by using ultrasonic probe. After that it was washed by using hot water (80^{o}C). Next, the suspension was filtered and dried at 70^{o}C by using oven for 20 hour and vacuum oven for 30 minutes. The dried sample was ground and sieved before being characterized by using X-ray Diffraction (XRD) and Field Emission Scanning Electron Microscope (FESEM). The steps were repeated to prepare samples under pH 5 and 6.

2.3 Characterization of sample

2.3.1 X-ray diffractometer analysis (XRD)

XRD analysis was performed to determine d-spacing of the bentonite samples by using X-Ray Diffractometer (XRD) Rigaku Mini Flex II Diffractogram. The scan rate used was 2^o/min in 2θ range of 1-15^o.

2.3.2 Field emission scanning electron microscope (FESEM)

FESEM analysis was done by FESEM Equipment (model:S-36; Carl Zeiss AG, Germany) with magnification 200000X to analyze the morphology of Bentonite before and after being treated with HNO_3.

3. RESULTS AND DISCUSSION

Figure 1 shows the FESEM images of the pristine

and destabilized Bentonites (b, c and d). The destabilized bentonites (b, c and d) have more loosely packed structure when compared to the pristine Bentonite (a). Larger interlayer spacing, greater porosity, smaller and more uniform platelets and clearer platelet edges can be seen throughout the micrographs, especially in the Bent-pH5/15 (c) sample. These were due to the destabilization and delamination effects by ultrasonication and pH changes by nitric acid treatment. Bendou and Amrani [5] also revealed that pH control through acid treatment has decreased the size of clay platelets.

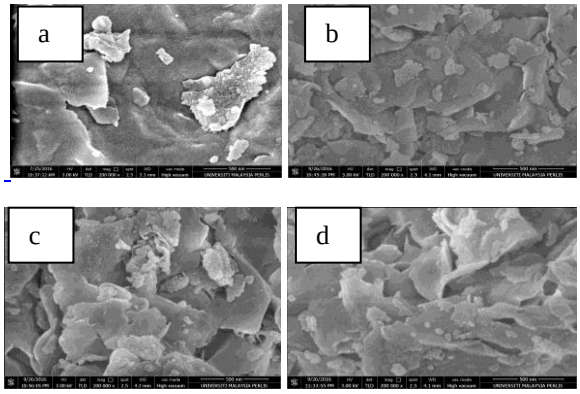

Figure 1 FESEM image of; a: Untreated Bentonite, b: Bentonite-pH4/15min, c: Bentonite-pH5/15min, d: Bentonite-pH6/15min.

As in Figure 2(b), d_{001} spacing for the pristine bentonite is 1.55nm. It is slightly lower than Bent-pH4/15 and Bent-pH6/15, in which both show the value of 1.57nm. However, Bent-pH5/15 has same d_{001}-spacing value with the pristine bentonite. Tombácz and Szekeres stated that when bentonite was treated with acid until the pH value reach lower than 6.5, the clay supposedly aggregates edge to face [6].The formation of edge to face structure are likely due to positive charge on the edge clay at low pH value and negative permanent charge at the clay surface [7].

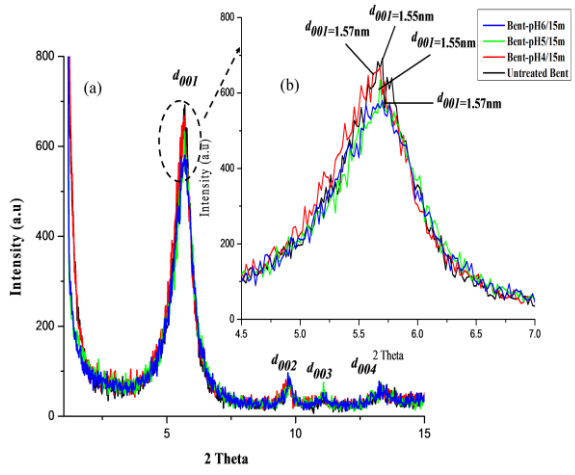

Figure 2 XRD pattern of the pristine and destabilized Bentonite powder (a) in 2θ range of 1°-15°, (b) in 2θ range of 4.5°-7° (d_{001} peak area).

As a result, the diffraction intensity decreases at low pH [6]. However, our results indicate no significant changes in both basal spacing and intensity upon the destabilization process. Therefore, further investigation will be done using lower scan rate and smaller 2 theta range to confirm the results.

4. CONCLUSION

The effect of destabilization process through ultrasonication and pH control on morphology of the Bentonite was studied. Nitric acid (HNO_3) was used to obtain the Bentonite suspension in different pH values (4, 5 and 6). Bentonite clay was characterized by FESEM and XRD. FESEM images show that the destabilization process creates a loosely packed tactoids. XRD analysis revealed that there was very slight different in basal spacing upon the destabilization process. Therefore, further analyses using different testing parameters and methods will be applied in future to allow more sensitive and accurate measurement.

ACKNOWLEDGEMENT

The authors would like to thank Ministry of Higher Education, Malaysia for funding the project through Fundamental Research Grant Scheme (FRGS) (No: 9003-00473).

REFERENCES

[1] A.S. Ahmed, Nsalehudeen, C.S. Ajimonoh, H. Hamza and A. Ohikere, "Studies on the mineral and chemical characteristics of pindinga Bentonitic Clay," *Petroleum Tech. Devel. Journal*, vol.1, pp.1-8, 2012.

[2] F. Piscetili, P. Posocco, R. Toth, M. Fermeglia, S. Pricl, G. Mensitieri, and M. Lavorgana, "Sodium Montmorillonite silylation : Unexpected effect of the aminosilane chain length,"*J. Colloid Interface Sci*, vol. 351, no.1, pp. 108-115, 2010.

[3] T. Missana and A. Adell,"On the Applicability of DLVO Theory to the prediction of Clay Colloids Stability," *J. Colloid Interface Sci*, vol. 230, no. 1, pp. 150-156, 2000.

[4] M.H. Baik and S.Y. Lee, "Colloidal stability of bentonite clay considering surface charge properties as a function of pH and ionic strength," *Journal of Industrial and Engineering Chemistry*, vol. 16, no.5, pp.837-841, 2010.

[5] S. Bendou and M. Amrani, "Effect of Hydrochloric Acid on the Structural of Sodic-Bentonite Clay," *Journal of Minerals and Material Characterization and Engineering*, vol.2, pp. 404-413, 2014.

[6] E. Tombácz and M. Szekeres, "Colloidal behavior of aqueous montmorillonite suspensions: the specific role of pH in the presence of indifferent electrolytes," Applied Clay Science, vol. 27, no. 1-2, pp. 75-94, 2007.

[7] J. Liu and I. Nertnieks, "Physical and chemical stability of the bentonite buffer," Report of Chemical Engineering and Technology, Royal Institute of Tecnology, Stockholm, Sweden, R-06-103, 2006.

Superhard carbon coatings and boundary lubrication

V. Levchenko[1,*], I. Buyanovsky[2], K. Zakharov[2], A. Bol'shakov[2], V. Matveenko[1]

[1)] Department of Colloid Chemistry, Lomonosov Moscow State University, Leninskii Gory 1, Moscow, 119991 Russia
[2)] Department of tribology, Blagonravov Mechanical Engineering Research Institute, Moscow, Russia

*Corresponding e-mail: vladalev@yahoo.com

Keywords: Superhard carbon coatings; DLC coatings-orientants; boundary lubrication

ABSTRACT – The monocrystalline carbon coating was originally prepared by the ion-assisted deposition method. It is shown that the composition and structure of diamond like carbon (DLC) coatings with monocrystalline structure have a substantial effect on the degree of the orientation of molecules of a lubricant in a boundary film.

1. INTRODUCTION

According to United Nations data, up to 30% of energy produced throughout the world is spent on overcoming friction in machines. This gives rise to increased fuel consumption, which leads to substantial losses of nonrenewable energy resources. A traditional method for reducing these losses is to develop energy and resource saving lubricating oils, which ensure the reduction of friction losses and a decrease in the accompanied wear of rubbing parts due to the optimization of viscosity and thermal characteristics of these oils during fluid film lubrication and the introduction of additives of various purposes into their composition. For example, the concentration of additives is 6–25% in diesel oils and 8–12% in transmission oils; from this amount, up to 5–7% of additives are intended to enhance the lubricity of the oils. These additives act under boundary lubrication conditions and give rise to improved antifriction and antiwear properties of oils. Many of the additives are expensive products. In addition, they often include compounds of elements (sulfur, chlorine, phosphorus, their compounds, etc.) that have a negative effect on the environment in the course of production, storage, use, and disposal [1]. One of the ways to reduce the negative effect of lubricating oils with additives is to decrease the concentration of active elements in additives or the replacement of more environmentally dangerous elements with less dangerous, although these components can hardly be eliminated. We propose an alternative method for enhancing the lubricity of oils based on peculiarities of the adsorption of molecules of a lubricant on friction surfaces which should be covered with DLC orienting coatings; in addition to orienting ability, these coatings possess high hardness and wear resistance [2-4]. The aim of this work was to assess the efficiency of the lubricity of a boundary film formed on an orienting coating as an alternative to a boundary film produced by introducing special additives into lubricants. Over the last decades, researchers from various countries have shown the efficiency of the deposition of carbon DLC on working surfaces of rubbing parts of lubricated friction joints for various applications. Such modification of surfaces ensures the extension of the life of tribo joints under conditions of oil starvation, makes it possible to transit from the boundary and mixed to the EHD lubrication mode, as well as reduces friction coefficients and the wear rate [4]. The objective of this study is a cordially new kind of DLC, i.e., a carbon orienting coating. This coating ensures the formation of a highly ordered homeotropically oriented layer of molecules on friction surfaces, which protects the surfaces against wear and scoring under friction, as well as reduces friction losses equally well with the traditional use of tribological additives. In this study, optimum structures and compositions of the carbon coating were assessed; a comparison of the friction of this coating against steel with the friction of steel against steel under various loads and at various frequencies of oscillations under boundary lubrication was carried out; and the effect of typical surfactant additive and chemically active additive on the tribological behavior of the steel - DLC pair was investigated.

2. METHOD FOR DEPOSITING COATING

To verify experimentally this assumption, a method for depositing carbon coatings on friction surfaces of steel specimens was developed. A highly ordered homeotropically oriented boundary lubricating film was produced using a special method for depositing a monocrystalline carbon coating (M-Carbon) with a highly ordered structure on steel surfaces. For comparison, an amorphous DLC coating (A-carbon) was tested. Both coatings were deposited using ion-plasma synthesis. Amorphous DLC carbon films with an amorphous structure were produced using the pulsed condensation of carbon plasma (ρ = 1013 cm–3, the degree of ionization was 95%) at τ = 400 μs and ν = 1–3 Hz. monocrystalline carbon films 3 μm thick were produced using the pulsed condensation of carbon plasma in combination with additional irradiation by Ar+ ions [2-4]. According to the Auger spectroscopy data, the films consist 99% of carbon. The density of electron states in the valence band corresponds to the calculated spectrum of carbon polymer with cumulated bonds. The Raman spectrum of the film contains the bands at 2100 and 2300 cm–1, which are typical of carbon polymer with a monocrystalline structure. The maximum Vickers hardness of the films (9800) is attained at energy of carbon atoms of 80 eV, which corresponds to the maximum probability of the recharge

of C+ ions on carbon clusters [2,5]. The examination of the carbon surfaces by electron diffraction has shown that the monocrystalline coating is highly ordered and ensures the formation of a highly oriented boundary film on the steel surface, while amorphous carbon does not ensure this orientation [3]. Therefore, carbon polymer with the regular linear-chain structure actually forms the surface layer whose elements are highly ordered, and this structure is reproduced by the boundary film.

3. RESULTS AND DISCUSSION

The effect of the alloying of carbon coatings during friction in base oils on their lubricity as applied to traditional DLC has been extensively studied. It was previously shown that the alloying of monocrystalline carbon coatings with nitrogen improves antifriction properties of model oils, while alloying with silver impairs these properties. On the other hand, some authors showed that the alloying of traditional DLC coatings with tungsten reduces the friction coefficient fairly efficiently in the case of lubricants containing sulfur, since tribochemical reactions that occur on friction surfaces lead to the formation of tungsten disulfide, which ensures the antifriction and antiwear effects. A question arose: will the alloying of the monocrystalline orienting coatings we developed with tungsten enhance the lubricity of oils? To this end, plate specimens for testing in the oscillating friction machines were produced; the top surfaces of the plates were coated with monocrystalline carbon coatings alloyed with tungsten (T-SCC). The analysis of the experimental results showed that the monocrystalline carbon coating alloyed with tungsten noticeably reduces the friction coefficient under the applied loads almost over the entire tribotest duration. In the entire range of the loads, the wear of coated steel is substantially lower than that of uncoated steel. For clarity, Figure 1 shows the microphotos of the surfaces of the plated specimens with the T-SCC coating Figure 1a and without coating Figure 1b. It follows from Figure 1a that the lines of grinding of the steel plate covered with the coating are not damaged; therefore, the nanocoating reliably protects the steel plate against wear.

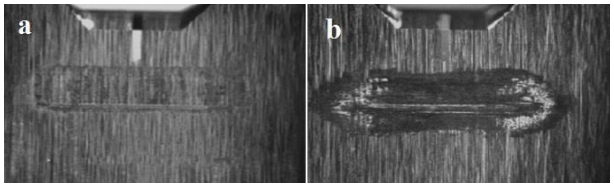

Figure 1 Microphotos of wear track on plate (a) with and (b) without coating after tests carried out under maximum load of 51N at frequency of oscillations 1Hz.

We failed to estimate the wear of the coating itself, since it is transparent. On the uncoated specimen, signs of wear are clearly seen; in the vicinity of the "dead points," signs of seizure are observed, i.e., the mechanisms of the wear of the steel specimens with and without the carbon coating substantially differ. It can be seen in the AFM image of the topography of the surface with the SCC alloyed with tungsten that the wear of the coating is accompanied by the smoothing of asperities and the spalling of the coating to a depth of ~300 nm.

4. SUMMARY

It has been shown that the deposition of hard carbon DLC on the working surfaces of solids, depending on their structure and composition determined by the deposition method, has a pronounced effect on the structure of boundary lubricating films, on the degree of the orientation of molecules of the lubricant in these films and, therefore, on tribological characteristics of friction units under boundary and mixed lubrication.

An analysis of the above-mentioned experimental results obtained using three testing machines with different contact geometries under various loads and at various frequencies of oscillation in three inactive lubricants (Vaseline oil, n-tetradecane, and PAOM-4) allows us to assert with a fairly high probability that the deposition of the monocrystalline carbon orienting coatings (including the coatings alloyed with tungsten) on friction surfaces substantially enhances both antifriction and antiwear properties of base lubricants and can be recommended for working surfaces of parts of heavy-duty friction units.

The order of the antifriction and antiwear characteristics of the boundary lubricating films formed on the orienting coating is close to that of the characteristics of the boundary films produced by introducing the tribologically active additives into the lubricant. The combined use of the monocrystalline carbon orienting coatings and the tribologically active additives (surfactant and chemically active) in our experiments has not revealed a noticeable effect.

REFERENCES

[1] V.A. Levchenko, I.A. Buyanovskii, I.A., et al., *Modern tribology: Results and Trends*, K.V. Frolov, K.V., Ed., Moscow, LKI, 2008.

[2] I.A. Buyanovskii, Z.V. Ignatieva, V.A. Levchenko, V.N. Matveenko, "Orientation ordering of boundary layers and lubricity of oils," *Journal of Friction and Wear*, vol. 29, no. 4, pp. 282-287, 2008.

[3] V. Levchenko, I. Buyanovsky, A. Bolshakov, V. Matveenko, "Green tribology: Influence of new DLC coatings-orientants and amorphous on antifriction properties of lubricants," *Journal of Electrical Engineering*, vol. 2, pp. 39-48, 2014.

[4] V.A. Levchenko, I.A. Buyanovsky, A.N. Bolshakov, M.N. Zelensky, Z.V. Ignatieva, V.N. Matveenko, "Influence of structure and structure of carbon coatings on lubricant properties of synthetic oil," *Friction and Wear*, vol. 34, no. 5, pp. 470-474, 2013.

[5] V. Levchenko, I. Buyanovsky, K. Zakharov, A. Bol'shakov, V. Matveenko, "New generation carbon coatings with monocrystalline structure as the promising new method of oil lubricity increasing" in *Proceedings of Malaysian International Tribology Conference*, 2015, pp. 7-8.

Characterization of SBE waste on particles size for building materials application

N. Salleh, Z. Shamsudin*, J.M. Juoi

Faculty of Manufacturing Engineering, Universiti Teknikal Malaysia Melaka,
Hang Tuah Jaya, 76100 Durian Tunggal, Melaka, Malaysia.

*Corresponding e-mail: zurina.shamsudin@utem.edu.my

Keywords: Spent bleach earth; particle size; building material

ABSTRACT – The purpose of this study is to characterize the green resources which is spent bleach earth (SBE) by particle size analysis and chemical composition analysis. The particle size analysis was performed using Laser particle size analyzer Model Mastersizer 2000 (Malvern) and chemical analysis was conducted by using X-ray Fluorescence (XRF) Model X-Supreme 8000 Oxford Instrument. It was found that the particle size of SBE was in the minimum range of commonly used size in clay brick formulation and the SBE contained high silica sand (SiO_2) and alumina (Al_2O_3) which contribute about 54.34 wt. %. Therefore, it is showed that the SBE was suitable for building material application.

1. INTRODUCTION

Spent bleach earth (SBE) is well known as one of vegetable industrial waste has dramatically increased due to demanding usage in production oil. SBE used as an absorbance in the vegetable refineries process including from palm oil industries. In Malaysia, over 150,000 tonnes of SBE is estimated to be produced annually with more than 17 million tonnes of palm oil production [1]. Generally, it is predicted that the production of SBE waste around the world is 600,000 tonnes [2]. The current practice to dispose the high volume of SBE is through landfill. However, this disposal method is problematic due to the oil on surface area of the SBE particles which exposed to oxygen from the environment. Thus, this will produce rapid oxidation and adequate heat to ignite the oil. Hence, the disposal activity need to be done immediately to avoid rapid oxidation. This disposal method has been banned by European Union (EU) landfill directive [3]. A consequence of this disposal method also was very costly and need to be paid by refineries [4]. Hence, alternative is extensively needed to control consequence mentioned. Recycling method can be used extensive in maintaining good levels in disposal of waste from refineries especially SBE.

The potential of SBE to be used as a clay substitute in the production of brick and tile manufacturing has been highlighted by many researchers [1,3]. Recent research on the formation of pore forming brick by Eliche-Quesada and Corpas-Iglesias [5] reported that only 10 wt. % of SBE was added into clay brick formulation that showed an optimum result of low bulk density, mechanical strength and thermal conductivity with higher total porosity and water absorption with respect to the pure clay brick.

Therefore, by analyzing the characterization of SBE in terms of particle size and chemical compositions on SBE, it is believed that more densified glass ceramic can be obtained as it will influence the sintering mechanism where the microstructure, mechanical and physical properties of the glass ceramic could be adjusted [6].

2. METHODOLOGY

A batch of spent bleach earth (SBE) has undergone a cleaning process to extract oil using sonification process followed by filtration and drying process until the SBE was in powdery form. The characterization of SBE were carried out by particle size analysis and chemical analysis.

The size of powder particles was measured using a Laser particle size analyzer Model Mastersizer 2000 (Malvern) version 5.54 Instrument. About 1gram of powder sample was added to the sample tray. The results were analyzed using Mastersizer Software.
The X-ray Fluorescence (XRF) analysis was conducted at Kolej Kemahiran Tinggi Mara (KKTM) Masjid Tanah Melaka. The analysis was carried out using X-Supreme 8000 Oxford Instrument. About 8 g of SBE powder added into pallet mold with diameter of 42 mm for pressing method. The compact pallet was formed by pressing using uniaxial dry pressing method with pressure of 2 tonnes. Then, the pallet sample was put into the sample holder for the analysis.

3. RESULTS AND DISCUSSION

The analysis of particle size and its frequency distribution indicates the amounts of that particular particle size exist in respective particle size intervals.

Figure 1 shows the distribution of particle size of SBE. The dominant size of SBE is in the range between 15 μm to 25 μm (69%) and 25 μm to 32 μm (31 %). These particle size is in the minimum range of commonly used size in clay brick formulation. The particle size is one of the important factor that affect the whole processing until achieving the properties of final product. Finer particle size, required shorter and lower sintering temperature [7]. The higher specific surface area of finer particle is also able to improve powder

flow ability and improve forming reactive material [8-9].

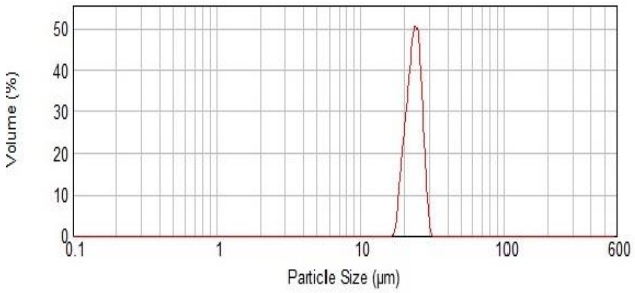

Figure 1 Particle size distribution of spent bleach earth (SBE)

Table 1 shows the chemical composition of SBE. The main element of SBE are silica sand (SiO_2) and alumina (Al_2O_3) which contribute about 54.34 wt. % which is suitable for clay substitute in building application. A significant amount of CaO and Fe_2O_3 was observed with approximately 6.649 and 4.949 wt. % respectively. The presence of Fe_2O_3 could provide a dark color towards sintered sample [5].

Table 1 Chemical composition of spent bleach earth.

Element	SBE (wt. %)
Al_2O_3	8.37
SiO_2	45.97
Na_2O	0.286
MgO	3.302
K_2O	1.250
CaO	6.649
TiO_2	0.772
Fe_2O_3	4.949
Cr_2O_3	0.0007
MnO_3	0.088
ZnO	0.001
P_2O_5	1.390
SO_3	0.448
Cl	0.044
SrO	-
LOI	26.48

A low proportion of other elements such as MgO, P_2O_5, K_2O and TiO_2 were also contained in SBE. Moreover, loss of ignition (LOI) for SBE is 26.48 wt. %. The above analysis is consistent with the finding from Mana et al. ; Eliche-Quesada and Corpas-Iglesias, [10,5] . The study by Eliche-Quesada and Corpas-Iglesias [5] on clay bricks found the LOI also quite high which was 53.5 wt. %. The cause of LOI was related to the dehydroxilation reactions, loss of humidity, carbonates decomposition and the combustion of organic matter present in clay. It was easily escape when heating, thus leaving pores inside and reduce the mass.

4. CONCLUSION

The characterization of spent bleach earth (SBE) in particle size analysis and chemical analysis reveal that the SBE was suitable to be used in building material application. It contained minimum range of commonly used particle size and has high silica sand (SiO_2) and alumina (Al_2O_3).

REFERENCES

[1] P.-L. Boey, S. Ganesan, G.P. Maniam, and D.M.H. Ali, "Ultrasound aided in situ transesterification of crude palm oil adsorbed on spent bleaching clay," *Energy Conversion and Management*, vol. 52, no. 5, pp. 2081–2084, 2011.

[2] S. Suhartini, N. Hidayat, and S. Wijaya, "Physical properties characterization of fuel briquette made from spent bleaching earth," *Biomass and Bioenergy*, vol. 35, no. 10, pp. 4209–4214, 2011.

[3] A. Beshara, and C.R. Cheeseman, "Reuse of spent bleaching earth by polymerisation of residual organics," *Waste management*, vol. 34, no. 10, pp. 1770–1774, 2014.

[4] S.K. Loh, S. James, M. Ngatimana, K.Y. Cheong, Y.M. Choo, and W.S. Lim, "Enhancement of palm oil refinery waste – spent bleaching earth (SBE) into bio organic fertilizer and their effects on crop biomass growth," *Industrial Crops and Products*, vol. 49, pp.775–781, 2013.

[5] D. Eliche-Quesada, and F.A. Corpas-Iglesias, "Utilisation of spent filtration earth or spent bleaching earth from the oil refinery industry in clay products," *Ceramics International*, vol. 40, no. 10, pp. 16677–16687, 2014.

[6] B. Cicek, A. Tucci, E. Bernardo, J. Will, and A.R. Boccacini, "Development of glass-ceramics from boron containing waste and meat bone ash combinations with addition of waste glass," *Ceramics International*, vol. 40, no. 4, pp.6045–6051, 2014.

[7] L.A. Pereira-de-Oliveira, J.P. Castro-Gomes, and P.M.S. Santos, "The potential pozzolanic activity of glass and red-clay ceramic waste as cement mortars components," *Construction and Building Materials*, vol. 31, pp.197–203, 2012.

[8] G. Matias, P. Faria, and I. Torres, "Lime mortars with ceramic wastes: characterization of components and their influence on the mechanical behaviour," *Construction and Building Materials*, vol. 73, pp. 523–534, 2014.

[9] M. Dondi, C. Iglesias, E. Dominguez, G. Guardini, and M. Raimondo, "The effect of kaolin properties on their behaviour in ceramic processing as illustrated by a range of Kaolins from the Santa Cruz and Chubut Provinces," *Applied Clay Science*, vol. 40, no. 1-4, pp.143–158, 2008.

[10] M. Mana, M.S. Oualia, L.C.D. Menorval, J.J. Zajacb, and C. Charnay, "Regeneration of spent bleaching earth by treatment with cethyltrimethylammonium bromide for application in elimination of acid dye," *Chemical Engineering Journal,* vol. 174, no. 1, pp. 275–280, 2011.

Processing and characterization of biodegradable polycaprolactone (PCL)/sago starch blends

M.S. Aludin*, T. Nur Hazwani

Faculty of Engineering Technology, Universiti Teknikal Malaysia Melaka,
Hang Tuah Jaya, 76100 Durian Tunggal, Melaka, Malaysia.

*Corresponding e-mail: aludin@utem.edu.my

Keywords: Polycaprolactone; sago starch; biodegradability

ABSTRACT – Polycaprolactone (PCL) is a commercially available biodegradable polymer. However, PCL is expensive and limited in resources. The objective of this study, therefore, is to blend PCL and sago starch at varied mass composition to lower the cost and increase biodegradability. The blends were prepared by employing solvent casting method. The thermal and mechanical properties of the blends were measured by Differential Scanning Calorimeter (DSC) and tensile test, respectively. The biodegradability of the blends was verified by soil burial biodegradation which following ASTM 988-12 method. The results show that the strength and ductility of the blends decreased with increasing starch content. The biodegradability of the sample films increased as the starch content were increased to 30% and then reached a plateau.

1. INTRODUCTION

Biodegradable polymers undergo chain cleavage due to the action of microorganisms and/or enzymes. From environmental perspective, biodegradable polymers provide an attractive alternative to conventional non-biodegradable polymers [1]. During the past two decades significant advances also have been made on biodegradable polymeric materials for biomedical applications [2].

Biodegradable polymers can be divided into two main groups; natural and synthetic. A promising class of synthetic biodegradable materials is the aliphatic polyesters such as poly(ε-caprolactone) (PCL), poly(hydroxy butyrate), poly(lactic acid), polybutylene succinate and poly(glycolic acid). Among them PCL is a particularly promising polymer [3]. PCL is prepared by ring-opening polymerization of ε-caprolactone, as shown in Figure 1.

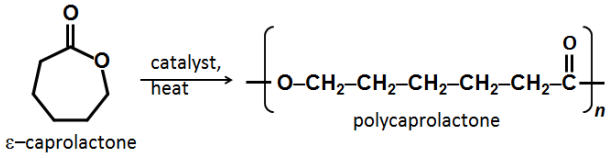

Figure 1 Ring-opening polymerization of ε-caprolactone.

Despite many atrractive properties, however, the applications of PCL have been restricted by its relatively high cost. Therefore, in this study, PCL was blended with cheap, abundant dan biodegradable sago starch as an attempt in producing biodegradable materials which are more cost competetive while retaining PCL's good thermal and mechanical properties, and biodegradability.

2. METHODOLOGY

2.1 Preparation of PCL/sago starch blends

The PCL having an average molar mass (M_n) of about 80,000 was supplied by Aldrich. The blends were prepared by using solvent casting method which involved two main processes; dissolution of PCL and sago starch in chloroform and solvent evaporation of the blends obtained.

2.2 Thermal Properties

The melting temperatures and the latent heats of fusion of the composites were measured by Differential Scanning Calorimeter (DSC). The DSC measurement was performed in the temperature range of 0 to 80°C at a heating rate of 10°C per minute under a constant stream of nitrogen at atmospheric pressure.

2.4 Mechanical properties

Ultimate tensile strength, yield stregth, Young's modulus and percent elongation at break were measured by an Instron tensile machine following ASTM D638-02a method. The crosshead speed was 50 mm/min.

2.5 Soil burial biodegradability test

The test followed ASTM 988-12 method. The sample films were buried in a multilayer substrate consisting of mineral/soil mixture and left for 10 days. Figure 2 show the biodegradability test set-up. The biodegradability was determined by measuring of the mass loss percentage of the samples after 10 days.

Figure 2 Soil burial biodegradability test set-up.

3. RESULTS AND DISCUSSSIONS

The range of melting temperatures and latent heats of fusion of the PCL/sago starch blends were 64.0~67.07°C and 28.0~51.2 kJ/kg, respectively. Based on the DSC curves, it can be concluded that no significant difference in the thermal properties among the blends indicating no chemical reaction occured between sago starch dan PCL chains.

Tensile test results revealed that increasing starch contents led to decreases in strength (ultimate and yield) and elongation at break. For example, the ultimate tensile strength and elongation percentage at break for PCL 50wt%/sago starch (SS) 50wt% blend were 1.35 MPa and 156%, respectively, which were much lower than that of pure PCL (ultimate tensile strength = 3.94 MPa, elongation percentage at break = 1528%). Table 1 tabulated the tensile test results.

Table 1 Tensile test results.

PCL/SS (wt. %)	Young's Modulus (MPa)	Utimate Tensile Strength (MPa)	0.1% Offset Yield Strength (MPa)	Elongation at Break (%)
100/0	13.3	3.9	1.3	1527
90/10	30.0	4.4	2.5	908
80/20	20.0	3.6	2.9	735
70/30	32.0	3.2	2.7	120
60/40	23.5	2.2	1.6	170
50/50	15.7	1.4	1.0	156

There is no clear observation on the effect of sago starch content on the Young's modulus of the blends. As overall, however, the addition of sago starch seems to increase the Young's modulus suggesting that the blends became stiffer. Sago starch that incorporated into polymer matrix still retains its granular shape after processing and led to the increase of the modulus because the starch granules are stiffer than polymer matrix [4].

The biodegradability of the PCL/sago starch blends was investigated based on the mass loss of the sample films after 10 days of soil burial biodegradability test. The mass losses of the films were ranged between 80 to 90%. The results are shown in Figure 3.

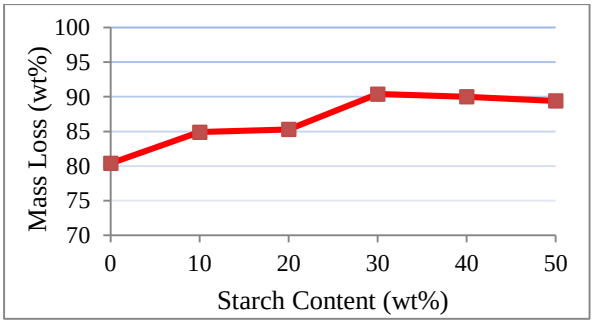

Figure 3 Mass losses of samples after 10 days.

The results clearly suggest that the biodegradability of PCL was enhanced significantly by incorporation of sago starch. However, increasing the starch content of the blends more than 30wt% produced no further enhancement in the blends biodegradability. Biodegradability of the sample films were also observed by Scanning Electron Microscope (SEM). Figure 4 shows the SEM micrographs of the blend containing 50wt% sago starch after 10 days biodegradation test.

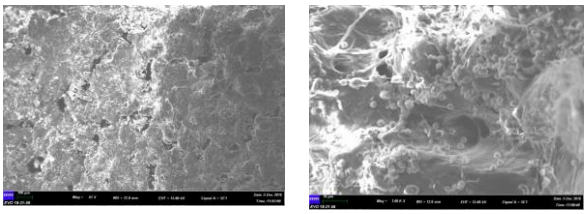

(a) 60 x magnification (b) 1000 x magnification

Figure 4 SEM migrographs of biodegraded sample.

There were many pores on the film surface indicating the occurence of biodegradation processes. The SEM micrographs also show that the sago starch particles with average size 2~5 μm in diameter were homogeneously dispersed throughout the PCL polymer matrix.

4. CONCLUSIONS

Blends of polycaprolactone (PCL) and sago starch, with starch contents to 50% mass composition, can be prepared by solvent casting method. Although the addition of starch lower tensile and yield strength, and the elongation of the blends, these materials show better toughness properties as compared to that of pure PCL. Moreover, the biodegradation test results revealed that the biodegradability of the blends also increased with increasing sago starch contents. These useful ranges of mechanical properties and biodegradability make these materials useful particularly in packaging, and also biomedical applications.

REFERENCES

[1] H. Shirahama, Y. Kawaguchi, M.S. Aludin, H. Yasuda, "Synthesis and enzymatic degradation of high molecular weight aliphatic polyesters," *Journal of Applied Polymer Science*, vol. 80, pp. 340-347, 2001.

[2] S.N. Lakshimi, T.L. Cato, "Biodegradable polymers as biomaterials," *Progress in Polymer Science*, vol. 32, pp. 762-798, 2007.

[3] J.A. Ratto, P.J. Stenhouse, M. Auerbach, J. Mitchell, R. Farrell, "Processing, performance and biodegradability of a thermoplactic aliphatic polyester/starch system," *Polymer*, vol. 40, pp. 6777-6778, 1999.

[4] S.A.A. Ghavimi, M.H. Ebrahimzadeh, M.A. Shokrgozar, M. Solati-Hashjin, N.A.A. Osman, "Effect of starch content on the biodegradation of polycaprolactone/starch composite for fabrication *in situ* pore-forming scaffolds," *Polymer Testing*, vol. 43, pp. 94-102, 2015.

Stiffness and fracture toughness behavior of kenaf fiber reinforced MWCNTs/epoxy multi-scale composites

N.A.M. Noor, J.A. Razak*, S. Ismail, N. Mohamad, I.S. Othman, H.T. Tew, M.Y. Yaakob

[1)] Carbon Research Technology Research Group, Advanced Manufacturing Centre, Faculty of Manufacturing Engineering, Universiti Teknikal Malaysia Melaka, Hang Tuah Jaya, 76100 Durian Tunggal, Melaka, Malaysia

*Corresponding e-mail: jeefferie@utem.edu.my

Keywords: MWCNTs; kenaf; multi-scale composite

ABSTRACT – This research was carried out to develop epoxy/kenaf/MWCNTs multi-scale composites system. The composites were produced by using a combination of hand lay-up technique and vacuum bagging process to enhance the desired end properties. A series of MWCNTs loading (0.00, 0.50, 1.00, 3.00, 5.00, 7.00 wt.%) were set to investigate their effects on the mechanical properties of produced composites. The fractured surface morphology of the selected sample was analysed by scanning electron microscopy (SEM) observation. The MWCNTs added to the epoxy at 1.00 wt.% were successfully enhanced the mechanical characteristic of hybrid multi-scaled composites of Kenaf-MWCNTS/epoxy composites about +63.63% and +90.52%, in term of their flexural and fracture toughness behavior, respectively.

1. INTRODUCTION

Active research focusing on the combination effects of natural fibre based composite and nanocomposite in single multi-scaled system are really scarce. Much works is still performed in searching a definite conclusion about the effects of nanofiller inclusion to the natural fibre reinforced polymer nanocomposite system. However, the lack of understanding for interfacial bonding between reinforcement and matrix resin are still becoming the main unsolved issues [1]. The technique to develop the nanocomposite is also an important parameter to produce a composite with a better property. This research aims to develop a kenaf fibre reinforced epoxy/MWCNTs multi-scale composites through a simplified hand lay-up and vacuum bagging process. MWCNTs nanofiller were embedded into the epoxy resin before being infused to the kenaf mat for multi-scale composites production. By embedding nanofiller into natural fibre based composites, the resulted end properties and performances could be tremendously improvised

2. METHODOLOGY

2.1 Raw materials preparation

Neat epoxy resin of (CP 360 Part A) and amine hardener (CP 360 Part B) are supplied by Terra Techno Engineering, Malaysia and used as received. The multi-walled carbon nanotube (MWCNTs, Flo Tub 9000 Series, CNano Technology Limited, China) was used without further treatment. The non-woven kenaf fiber supplied by Lembaga Kenaf & Tembakau Negara (LKTN), Malaysia was prepared and conditioned in-house. In this work, 80 grams of kenaf mat was used to fabricate multiscale epoxy/kenaf-MWCNTs composites.

2.2 Sample fabrication

A variation of 0.0 %, 0.5 %, 1.0 %, 3.0 %, 5.0 % and 7.0 % each of MWCNTs was mixed into epoxy and stirred by means of high speed mechanical stirring operation (1000 rpm, 60 minutes). The hardener agent CP360B with a ratio of 2, epoxy: 1, hardener was then poured into the mixture and manually stirred for 5 minutes before evenly impregnated on the fibre mat. The laminates are left to cure at ambient temperature for 24 hours before cut into specific dimension of 125x12.7x 3.2mm (*l x w x t*) required for flexural and span length of 80 mm for fracture toughness test, in accordance to ASTM D790 and ASTM D5045, respectively. The SEM observation was performed to observe the morphological fractured surfaces at 300x magnification.

3. RESULTS AND DISCUSSIONS

3.1 Flexural properties evaluation

The trend of flexural strength as depicted in Figure 1 was found increase with the increased of MWCNTs loadings up to 1.00 wt. % filler, before it decreased afterwards. At 1.00 wt. % of MWCNTs addition, the multi-scaled composites had shown the highest flexural strength of 53.67 MPa which about 63.63 % higher improvement compared than unfilled epoxy/kenaf composite. The MWCNTs added at 1.00 wt. % are optimally dispersed throughout the kenaf fiber and provide a better adhesive bonding between the matrix and reinforcement. Therefore, the stress are effectively transferred to the kenaf fiber [2]. In contrast, at 7.0 wt. % of MWCNTs multi-scaled composites had shown the lowest performance of flexural strength. The flexural strength is about 18.08 MPa with 44.88 % lower than of kenaf-epoxy composites without MWCNTs addition. This is because of enhanced viscosity of nanocomposites which lead the MWCNTs to form a largest agglomeration that tend to be the weakness point within composites [3].

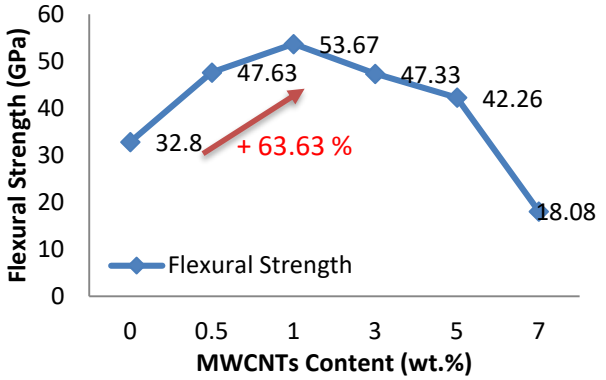

Figure 1 Effect of MWCNTs content on flexural strength of epoxy/kenaf-MWCNTs multi-scale composite.

3.2 Fracture toughness evaluation

Fracture toughness of multi-scale kenaf fibre reinforced MWCNTs-epoxy hybrid composites were measured by three-point bending test and the obtained results were plotted as a function of weight percentages of MWCNTs loadings as could be seen available in the Figure 2. According to Chandrasekaran et al. [4], the fracture toughness of composite will start to decrease beyond certain weight fraction of filler addition which is in parallel with the results found in this study. Figure 2 shows that the fracture toughness was increased when the addition of MWCNTs increased up to 1.00 wt. %. Later, more addition of MWCNTs cause a lower performance of resulted composites. It is noticed that the addition of 1.00 wt. % of MWCNTs provides the highest fracture toughness value of 86.39 MPa$\sqrt{m}$ with 90.52 % improvement as compared than unfilled kenaf/epoxy composite system. This is due to the increase of MWCNTs content which tends to form agglomeration that diminish the quality of produced composite [5]. Moreover, the agglomeration of MWCNTs tend to act as crack initiation point which later propagated throughout the sample which resulted the fracture of composite [4].

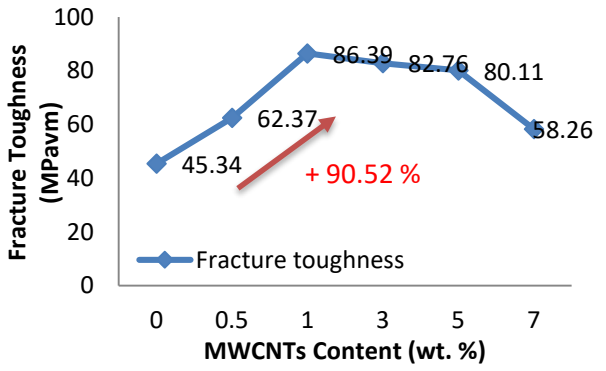

Figure 2 Effect of MWCNTs addition on fracture toughness behaviour of epoxy/kenaf/MWCNTs multi-scale composite.

3.3 Morphological observation

Fracture micrograph in Figure 3 represents the fractured surface of epoxy/kenaf/1.00 wt. % MWCNTs multi-scale composite. According to Garg et al. [6], the higher the MWCNTs loading, the tendency of higher agglomeration are expected in response to the increase of epoxy viscosity. The micrograph shows the fibre breakage rather than being pulled out from the epoxy matrix. This occurrence indicates that the matrix-filler interface is stronger which promote a better strength. Furthermore, a good dispersion of MWCNTs in epoxy was found to reduce the stress concentration which further enhanced the uniformity of the stress distribution of produced hybrid multi-scaled composites [7].

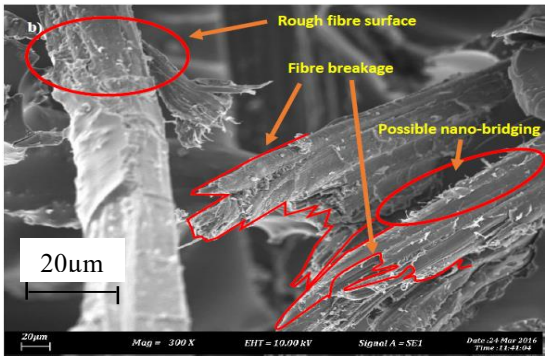

Figure 3 SEM micrograph of epoxy/kenaf/1.0 wt. % MWCNTs nanocomposite at 300x magnification.

4. CONCLUSIONS

In a nut-shell, it shows that the addition of MWCNTs at different wt. % loadings are influenced the end properties of produced multi-scale kenaf fibre reinforced epoxy/MWCNTs composites. The flexural strength and fracture toughness behaviour of sample with 1.00 wt. % of MWCNTs addition had yielded a significant improvement by 63.63 % and 90.52 %, respectively.

ACKNOWLEDGEMENT

We greatly acknowledged the research funding from Research Acculturation Grants Scheme coded RAGS/1/2014/TK04/FKP/B00072 from the Ministry of Higher Education, Malaysia.

REFERENCES

[1] E.T. Thostenson, C. Li and T.W. Chou, "Nanocomposites in context," *Composites Science and Technology*, vol. 65, pp. 491–516, 2005.

[2] M.T. Kim, K.Y. Rhee, J.H. Lee, D. Hui and A. K. T. Lau, "Property enhancement of a carbon fiber/epoxy composite by using carbon nanotubes," *Compos. Part B Eng.*, vol. 42, no. 5, pp. 1257–1261, 2011.

[3] L. Yue, G. Pircheraghi, S.A. Monemian and I. Manas-Zloczower, "Epoxy composites with carbon nanotubes and graphene nanoplatelets - Dispersion and synergy effects," *Carbon N. Y.*, vol. 78, pp. 268–278, 2014.

[4] S. Chandrasekaran, N. Sato, F. Tölle, R. Mülhaupt, B. Fiedler and K. Schulte, "Fracture toughness and failure mechanism of graphene based epoxy composites," *Compos. Sci. Technol.*, vol. 97, pp. 90–99, 2014.

[5] J.M. Wernik and S.A. Meguid, “On the mechanical characterization of carbon nanotube reinforced epoxy adhesives,” *Mater. Des.*, vol. 59, pp. 19–32, 2014.

[6] P. Garg, B.P. Singh, G. Kumar, T. Gupta, I. Pandey, R.K. Seth, R.P. Tandon and R.B. Mathur, “Effect of dispersion conditions on the mechanical properties of multi-walled carbon nanotubes based epoxy resin composites,” *J. Polym. Res.*, vol. 18, no. 6, pp. 1397–1407, 2011.

[7] A. Montazeri, J. Javadpour, A. Khavandi, A. Tcharkhtchi, and A. Mohajeri, “Mechanical properties of multi-walled carbon nanotube / epoxy composites,” *Mater. Des.*, vol. 31, no. 9, pp. 4202–4208, 2010.

Utilizing digital image correlation method in assessing deformation of composite under tensile and bending

A.F. Ab Ghani*, W.S. Wan Harun, F.K. Zahari, M.H. Zakari, M.J. Juki

Faculty of Mechanical Engineering, Universiti Teknikal Malaysia Melaka,
Hang Tuah Jaya, 76100 Durian Tunggal, Melaka, Malaysia

*Corresponding e-mail: ahmadfuad@utem.edu.my

Keywords: Digital image correlation; composite; tensile; bending

ABSTRACT – The article presents experimental approach using digital image correlation on measuring in plane strain from tensile test and deflection from bending test of composite Carbon Fiber Reinforced Polymer (CFRP) and Glass Fiber Reinforced Polymer (GFRP). The value of E11, obtained from both methods with the utilization of DIC proves that the technique is reliable tool for measuring deformation of composite material and can be further use for other complex material behavior and loading.

1. INTRODUCTION

The major challenge for the composite engineer is to develop of new stronger, tough and lightweight materials to supporting the latest design concept for complex shape structural. Composite are attractive material because of their properties such as high strength and stiffness leads to application in the area marine, aerospace and automotive. A composite material also can be defined as a combination of a matrix and reinforcement [1]. Tensile test is one of the mechanical testing that evaluating fundamental properties of engineering materials as well as in developing new materials and in controlling the quality of materials for use in design and construction. The main parameter that can obtain during the tensile test is Ultimate Tensile Strength (UTS), Yield Strength (σ_y), Elastic Modulus (E), Poisson Ratio (v), and percent elongation percent elongation (ΔL) [2]. The standard method for tensile testing polymer matrix composites was described by ASTM D3039 [1]. Apart from that, flexural and bending behavior of composite material can be assessed by performing using three-point bending test.

2. METHODOLOGY

Several coupons tensile and bending for CFRP and GFRP have been prepared using hot press machine at specified pressure of 6bar atm and 120 degree Celsius for 1 hour duration. Both type of coupons was prepared as accordance to ASTM D3039 as shown in Figure 1.

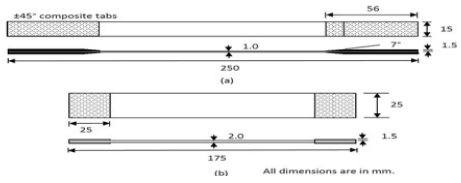

Figure 1 Composite tensile test coupon ASTMD3039.

Table 1 Material Database for CFRP and GFRP.

Properties	CFRP	GFRP
E_1 (GPa)	128.8	45.2
E_2 (GPa)	9.3	14.1
V_{12}	0.34	0.29
G_{12} (GPa)	3.37	6.3

Manufacturer data for material under study as shown in Table 1 are taken from Toray. The tensile test was performed on CFRP and GFRP at a rate of 2mm/min while for bending testing was done at 1mm/min. At each interval of load specified before test, images were taken on in plane surface of tensile test and bending test deflection. The images then stored for later analysis that correspond to certain load for stress strain relationship and deflection against load for bending.

2.1 Setting up of digital image correlation technique

The features contain the sensor recording speeds of up to 200,000fps and 800 x 600 resolutions at 1000fps, Camera Display Unit (CDU) built in measurement, and storage and editing capability. Olympus I-Speed 3 camera is used to capture images for tensile and bending test. DIC system use optic method through stereoscopic sensor arrangement to analyze the deformation of object and emphasis on each point subset based on grey value of digital image to define the strain [3,4]. The camera is positioned perpendicular to the specimen under testing [Figure 2]. In order for the digital image correlation algorithm able to perform the correlation analysis, speckle pattern must be sprayed onto the surface of the coupon [Figure 3]. The pattern must be contrast enough and small enough to capture the deformation [5]. The technical specification of the high speed camera is as follow: Frequency 60 – 200,000 fps; Shutter minimum of 1 micro second.

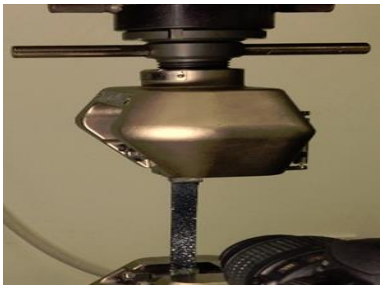

Figure 2 High speed camera capturing tensile coupon.

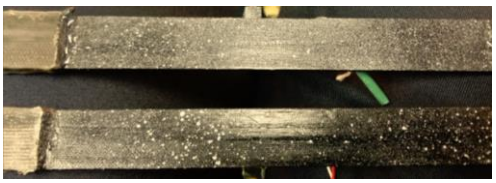

Figure 3 Speckle pattern sprayed onto gauge region.

3. RESULTS AND DISCUSSION

Post processing series of images acquired by high speed camera then analyzed using open source DIC program, Ncorr. The algorithm of the software will derive strain yy,xx and xy (shear) from derivative of displacement at respective direction[Figure 4].

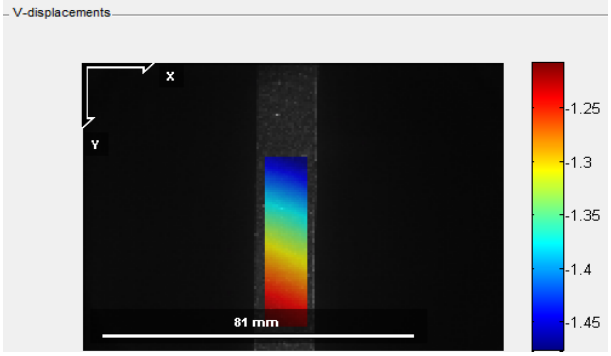

Figure 4 Contour of displacement in at 5000N (CFRP).

The strain in yy direction which equates longitudinal direction was then obtained via derivative of displacement in yy (Figure 5).

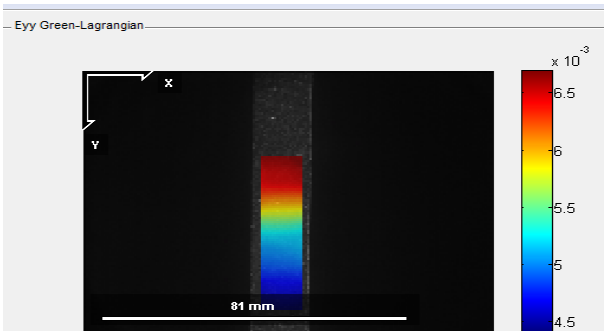

Figure 5 Strain contour, ε_{yy} at 5000N (CFRP).

Figure 6 shows image of CFRP taken by high speed camera at specified load of 160N. As for bending test performed as accordance to ASTM D7264, DIC method in this study will just compute deflection. Other capability of DIC with advanced micro lense able to capture strain on through thickness of bending specimen which is not covered in this project.

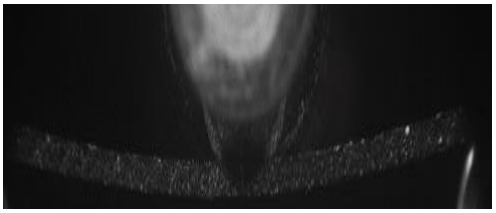

Figure 6 Deformed specimen corresponding to 160N bending test.

$$E = \left[\frac{F}{\Delta}\right].\frac{L^3}{48.I} \quad (1)$$

Where: F = the applied vertical load at mid-span; L = the span or the distance between supports; A = the cross-section area; I = the inertia moment of the section with respect to the y axis; E = the flexural elastic modulus or Young longitudinal modulus for isotropic material; G = the shear modulus; $[F/\Delta]$ = slope of the tangent to the initial straight-line portion of the load deflection curve, N/mm] of deflection. Deflection within the range of 1.7-1.75mm was obtained from bending test which correspond to 160N. The values inserted into Eq 1 yields the E equals 117 GPa which validates the value obtained from stress strain plot from tensile test of CFRP which equates 109GPa (Figure 7).

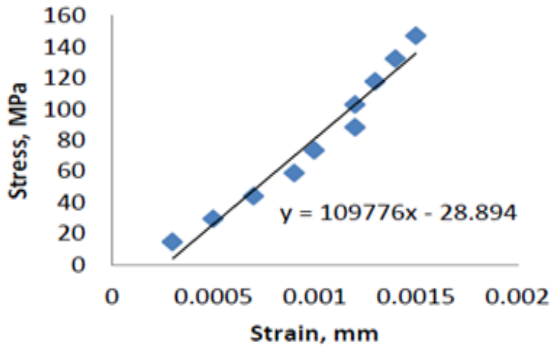

Figure 7 Stress strain plot for tensile(CFRP) using DIC.

4. SUMMARY

The use of digital image correlation technique with high speed camera to measure in plane strain and bending deformation of composite material have been performed. Open source software 2D DIC Ncorr version 1.2 is able to post process output in the form of in plane strain longitudinal, transverse and shear as well as bending deflection (displacement). Value of modulus of elasticity, E_{11} in longitudinal direction obtained for CFRP and GFRP match the literature and manufacturer data sheet values. Deflection of beam from bending testing is obtained from high speed camera and deflection is calculated from DIC as input for equation for findings, E (modulus of elasticity).

ACKNOWLEDGEMENT

Authors would like to thanks Faculty of Mechanical Engineering, Universiti Teknikal Malaysia Melaka (UTeM) for tensile testing facility and high speed camera, Olympus i-SPEED 3 high speed camera. This research is funded under UTeM's Grant PJP/2015/FKM(1A).

REFERENCES

[1] Chung, D.L. Deborah, *Composite Materials*, Springer-Verlag London, 2010.
[2] Ochsner, Andreas, da Silva, F.M. Lucas, Altenbach, Holm, *Mechanics and Properties of Composed Materials and Structures*, Springer, 2012.
[3] J. Blaber, B. Adair, A. Antoniou Ncorr, "Open-source 2D digital image correlation matlab

software," *Exp Mech*, vol. 55, no. 6, pp. 1105–1122, 2015.

[4] B. Pan, K. Qian, H. Xie, A. Asundi, "Two dimensional digital image correlation for in-plane displacement and strain measurement: A review," *Measurement Science and Technology*, vol. 20, no. 6, 2009.

[5] M.A. Sutton, J.J. Orteu, H.W. Shreier, *Image Correlation for Shape, Motion and Deformation Measurements,* Springer, New York, US, 2009.

Effect of dispersant concentration on morphology of the ultrasonicated organically modified montmorillonite

Asna Rasyidah Abdul Hamid[1], Azlin Fazlina Osman[1,*], Darren Martin[2], Yusrina Mat Daud[1], Mustafa Al Bakri Abdullah[1], Che Mohd Ruzaidi Ghazali[1]

[1)] Center of Excellence Geopolymer and Green Technology, School of Materials Engineering, Universiti Malaysia Perlis, Kompleks Pusat Pengajian Jejawi 2, Taman Muhibbah, 02600 Jejawi, Perlis, Malaysia
[2)] Australia Institute for Bioengineering and Nanotechnology (AIBN), University of Queensland, Australia.

[*]Corresponding e-mail: azlin@unimap.edu.my

Keywords: Ultrasonication; organo-montmorillonite; exfoliation

ABSTRACT – The production of fully exfoliated polymer/clay based nanocomposites is crucial to obtain an actual benefit of nanoscale reinforcement in the polymer matrix. In fact, nanoclay dispersion is a key to enhance overall polymer nanocomposite properties. In this study, ultrasonication was employed as a method to exfoliate and disperse organically modified montmorillonite (OMMT) platelets prior to melt compounding with polymer matrix. The effect of dispersant concentration during the ultrasonication process on morphology of the OMMT was investigated. The suspensions of OMMT/distilled water (H_2O) were prepared by ultrasonication using different dispersant concentrations (OMMT:H_2O = 1:5, 2:5, 3:5, 4:5, and 1:1). The morphology of the ultrasonicated OMMTs were characterized by using Field Emission Scanning Electron Microscope (FeSEM) and X-Ray Diffraction (XRD) technique. The results suggest that the OMMT platelets were more exfoliated and dispersed upon the ultrasonication process. The OMMT:water ratio of 1:1 resulted in the best dispersing/exfoliating effect.

1. INTRODUCTION

Research on nanoclay/polymer nanocomposites has greatly attracted scientists due to the fact that polymer nanocomposite can perform greatly enhanced mechanical and physical properties as compared with conventional polymer composites. A relatively small amount of nanoclays, typically in the range of 3–5 wt%, is enough for the enormous improvements in the mechanical and thermal properties of the host polymer. The presence of exfoliated or intercalated nanoclay in a polymer matrix can not only enhance the mechanical, thermal, barrier properties and biostability but also can potentially improve its biocompatibility [1-3].

Organically modified clays (organo-clays) were widely used as nanofiller in the production of polymer nanocomposite. They are produced through surface modification of the pristine clays using organic surfactants, to render the clay surface hydrophobic. This was done to ensure compatibility of the nanoclay with the hydrophobic polymer matrix. Among all the organoclays, the most commonly used is the organo-MMT (OMMT). The incorporation of the OMMTs in polymer matrices has resulted in enhancement in mechanical, physical and thermal properties of the host polymers. Osman et al., [2] applied the OMMT as nanofiller in the ethyl vinyl acetate (EVA) copolymer. Significant enhancement in tensile properties of the EVA was obtained when low loading (1 & 3 wt%) of the OMMT was employed. However, when higher loading (5 wt%) were added, reduction in tensile properties were observed due to reduced quality of the OMMT dispersion and exfoliation in the EVA matrix [2]. As a continuation of this study, our present investigation deals with pre-dispersing technique using ultrasonication to improve the dispersion and exfoliation of the OMMT nanofiller. The aims were to allow the improvement in OMMT exfoliation and dispersion when higher loading of these nanofiller (greater than 3 wt%) were incorporated into the polymer. This is because; more significant thermal and biostability enhancement of the host polymer can be obtained if higher nanofiller content is added [1,4]. Furthermore, cytotoxicity of the OMMT can be reduced upon the ultrasonication process due to enhanced nanofiller delamination [3]. These findings have brought our interest to further study the effect ultrasonication parameters such as dispersant concentration, time and temperature on the morphology and properties of the OMMT and the resultant polymer nanocomposite. However, in this paper, we only report the effect of dispersant concentration on the morphology of the OMMT.

2. METHODOLOGY

The clay used was organically modified montmorillonite (OMMT), the same material used in previous studies [1,2]. Distilled water was used as ultrasonication medium to allow swelling of the OMMT. The OMMTs were prepared in suspension from using different ratio of OMMT and distilled water. The suspensions were homogenized using ultrasonic probe for five minutes at 20 kHz amplitude. Then, the resulting gel-like suspensions were placed in the oven for 48 h until fully dried.

The XRD analysis was performed using Phaser-D2 manufactured by Bruker company (X'Pert PRO) and run at room temperature with an angle range (2θ) from 10˚ to 30˚ at a scanning speed of 2°/min and step size of 0.02º using CuKα radiation operating at 45 kV. The surfaces morphology was observed using a (JOEL,

JSM-7800F, Japan) field emission scanning electron microscope (FeSEM). Samples were mounted on aluminum stubs with a carbon tape followed by a sputter coating with platinum at an accelerating voltage of 20 kV.

3. RESULTS AND DISCUSSION

Morphological changes of the OMMT upon the ultrasonication process were characterized using XRD analysis. Figure 1 displays XRD patterns of the pristine OMMT and ultrasonicated OMMT (OMMT/H_2O) with different water concentration ratios (1:5, 2:5, 3:5, 4:5, and 1:1).

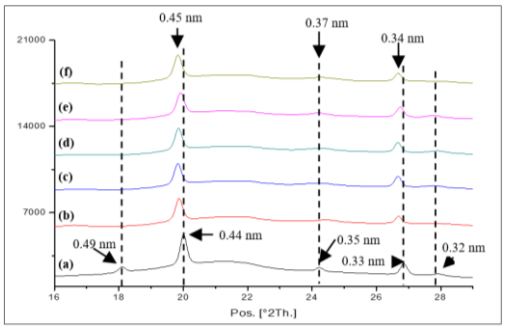

Figure 1 X-ray diffraction patterns of (a) OMMT, (b) OMMT/H_2O (1:5) (c) OMMT/H_2O (2: 5) (d) OMMT/H_2O (3:5) (e) OMMT/H_2O (4:5) (f) OMMT/H_2O (1:1).

It can be seen that the pristine and ultrasonicated OMMTs show several diffraction peaks. Five diffraction peaks were observable at 2θ = 18.08°, 19.99°, 24.22°, 26.83° and 27.91° in the pristine OMMT sample. Interestingly, the diffraction peak at 2θ = 18.08° (d_{001}) strikethrough disappeared upon the ultrasonication process due to the loss of crystallographic order [2]. Furthermore, the d_{002} and d_{004} peaks were shifted to lower 2θ angles, indicating expansion of the basal spacing due to swelling of the clay platelets. OMMT/H_2O (1:1) sample exhibits the largest basal expansion among all the ultrasonicated samples. In addition, the broadening of the peaks was observed which was also accompanied by reduction in peak intensity. These results indicate that the ultrasonication process has reduced the OMMT tactoid size by disrupting the ordering of the OMMT platelets. These effects were obtained through 'destabilization' of the OMMT interlayer cohesive energy by high energy sonic waves [3,4].

Figure 2 illustrates FeSEM micrographs of the pristine and ultrasonicated OMMT at 200,000X magnification. It is clearly evident that the pristine OMMT (figure 2a) exist as closed pack platelets with smooth surface and distinct bent edges [5]. In contrast, after the ultrasonication process, the curled, crumpled and bend edges morphologies disappeared, while the platelets stacked in more loosely packed structure. The ultrasonicated OMMT has formed porous-agglomerated structure due to enhanced platelet spacing and disorganization of the platelets.

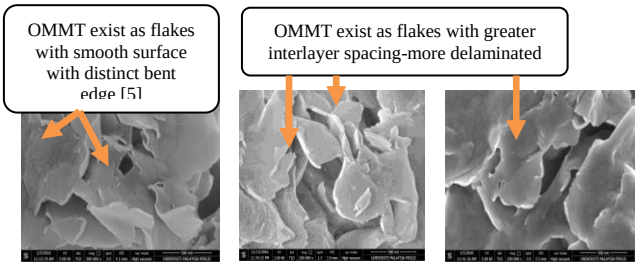

Figure 2 FeSEM images of (a) OMMT (b) OMMT/H_2O (1:1) (c) OMMT/H_2O (1:5) at 200,000X magnification.

4. CONCLUSIONS

This paper presents the ultrasonication effect using different dispersant concentration on the dispersion and platelet arrangement of the OMMT. The XRD patterns and FeSEM images provide direct evidence of exfoliation and delamination of the pre-dispersed OMMT. XRD and FeSEM analysis showed that the inter-layer spacing of the OMMT was increased upon the ultrasonication process. Disruption in platelets ordering resulted in smaller tactoid size and more loosely packed OMMT platelets.

ACKNOWLEDGMENTS

Grant no.: FRGS - 9003-00473.

REFERENCES

[1] A.F. Osman, A.R. Abdul Hamid, Md. Rakibuddin, G.K. Weng, R. Ananthakrishnan, S.A. Ghani, Z. Mustafa, "Hybrid silicate nanofillers: Impact on morphology and performance of EVA copolymer upon *in vitro* physiological fluid exposure," *Journal of Applied Polymer Science*, 133, pp. 44640-44655, 2016.

[2] A.F. Osman, A.M. Alakrach, H. Kalo, W.N.W Azmi, F. Hashim, "In vitro biostability and biocompatibility of ethyl vinyl acetate (EVA) nanocomposites for biomedical applications," *RSC Advances*, vol. 5, no. 40, pp.31485-31495, 2015.

[3] A.F. Osman, T.F.M. Fitri, Md. Rakibuddin, F. Hashim, S.A.T.T. Johari, R. Ananthakrishnan, R. Ramli, "Pre-dispersed organo-montmorillonite (organo-mmt) nanofiller: morphology, cytocompatibility and impact on flexibility, toughness and biostability of biomedical ethyl vinyl acetate (EVA) copolymer," *Material Science and Eng. C*, DOI: 10.1016/j.msec.2016.11.137, 2016.

[4] A.F. Osman, H. Kalo, M.S. Hassan, T.W. Hong, F. Azmi, "Pre-dispersing of montmorillonite (MMT) nanofiller: Impact on morphology and performance of melt compounded ethyl vinyl acetate (EVA)," *J. of Appl. Poly. Science*, vol. 133, no. 11, pp. 43204-43219, 2016.

[5] B. Pradhan, S. Roy, S.K. Srivastava, A. Saxena, "Synergistic effect of carbon nanotubes and clay platelets in reinforcing properties of silicone rubber," *J. of Applied Polymer Science*, vol. 132, 13, 41818, 2015.

Comparison of strut properties for micro-lattice structure manufactured using selective laser melting

R. Hasan[1,2,*], R.A.W. Mines[3]

[1)] Faculty of Mechanical Engineering, Universiti Teknikal Malaysia Melaka,
Hang Tuah Jaya, 76100 Durian Tunggal, Melaka, Malaysia
[2)] Centre for Advanced Research on Energy, Universiti Teknikal Malaysia Melaka,
Hang Tuah Jaya, 76100 Durian Tunggal, Melaka, Malaysia
[3)] School of Engineering, University of Liverpool, Liverpool L69 3GH, United Kingdom

[*]Corresponding e-mail: rafidahhasan@utem.edu.my

Keywords: Micro-lattice structure; additive layer; selective laser melting

ABSTRACT – This paper discusses on the micro-strut properties of titanium alloy Ti-6Al-4V micro-lattice structure manufactured using additive layer technology, selective laser melting (SLM). Micro-strut properties were determined from single-strut tensile test and micro-lattice block compression test analysis, and were compared to standard properties of titanium alloy material. The results show that strut Young's Modulus and ultimate stress which were determined using micro-lattice block compressive properties were comparable to that of standard value of titanium alloy material. This suggests that the strut properties derived from the micro-lattice blocks can be used in the estimation of individual micro-strut in the lattice structure material.

1. INTRODUCTION

It is reported that titanium alloy micro-lattice structure has a specific strength which is comparable to that of aluminium honeycomb [1]. However, the competition from aluminium alloys in terms of cost can affect the usage of titanium alloy in future. It is believed that the application of titanium alloy could be increased by investing in improved and advanced technology in production and manufacturing of the material. Since the titanium alloys can be manufactured from its powder form, the advanced technology of Selective Laser Melting (SLM) was found to be suitable to produce solid titanium parts directly from the metal powder [2]. Yet, there are many aspects to be explored in this advanced technology capabilities.

In research of SLM titanium alloy Ti-6Al-4V micro-lattice structure material, it is important to characterize the basic unit of the material, which is the micro-strut, in order to fully understand the properties and behaviours of the material. There is an interest to determine the single strut properties from the micro-lattice block and to compare it with that of individually manufactured strut. This is based on the suggestion by Hooputra et al. [3] which mentioned that the plastic deformation and failure of individual component parts is essential in the failure prediction of a structure. The findings from this study can be used in the estimation of performance for SLM titanium alloy Ti-6Al-4V micro-lattice structure material.

2. METHODOLOGY

Individually manufactured titanium alloy struts and micro-lattice blocks as shown in Figure 1 were manufactured using the SLM machine as described in other report [4]. The selected parameter was 160 W laser power and 1000 μs laser exposure time.

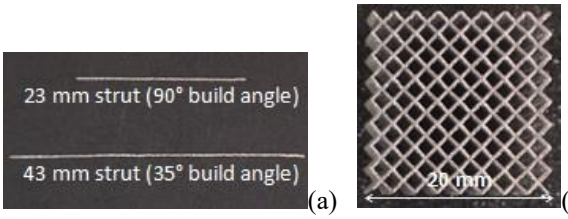

(a) (b)

Figure 1 (a) Individually manufactured struts (b) Side view of micro-lattice structure block.

Tensile test was carried out on the individually manufactured struts and compliance correction method (ASTM D 3379-75) was applied in the analysis of strut properties [5]. The Young's Modulus and ultimate stress values were determined from stress-strain curve that obtained from the test.

Meanwhile, uniaxial quasi-static compression test was conducted on micro-lattice structure blocks, with lubricated compression platens and crosshead displacement rate at 0.25 mm/min [4]. Stress-strain curve from this test has given the maximum stress and stiffness values of the micro-lattice block. These values together with strut diameter value that was derived earlier [6] were then used in the determination of the properties of the strut in the block.

The properties of strut that were determined from both tensile and compressive tests were compared to that of standard properties for titanium alloy Ti-6Al-4V material [7].

3. RESULTS AND DISCUSSION

Figure 2 shows the stress-strain curve that was derived from tensile test of the individually manufactured strut. The strut properties were determined using the nominal value of strut diameter which was 0.375±0.004 mm. The upper range and lower range boundaries were plotted based on the maximum and minimum range of diameter values. Meanwhile,

0.2% proof stress was applied to determine the yield strength (YS) property. The true stress-strain was derived [4] and plotted in tandem with the engineering stress-strain curve in order to observe the similarity pattern between both curves.

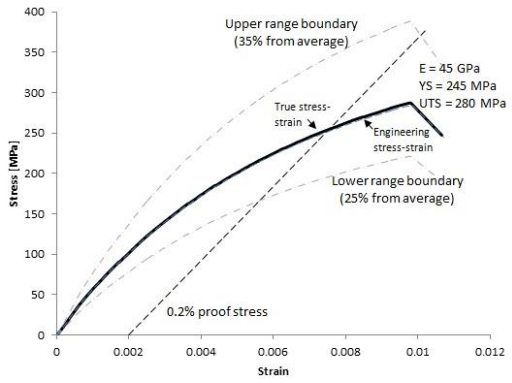

Figure 2 Stress-strain curve from tensile test of the individually manufactured strut.

On the other hand, Table 1 lists the summary of micro-lattice structure block properties, obtained from compression test results.

Table 1 Summary of micro-lattice block result (160 W by 1000 µs).

Properties	**Data**
Max. stress, $\sigma_{micro\text{-}lattice}$	7.4 MPa
Stiffness, $E_{micro\text{-}lattice}$	96.8 MPa
Estimated diameter, d	343 µm
Unit cell length, L	2.5 mm

The maximum stress and stiffness values of micro-lattice blocks were applied in Equation 1 and Equation 2 below, which were based on re-arranged theoretical work of Ushijima et al. [8] in terms of the properties' arrangements as well as the nomenclatures for simplification of current research.

$$E_{strut} = \frac{E_{micro-lattice}}{\sqrt{3}\,\pi} \cdot \frac{1+2(L/d)^2}{(d/L)^2} \quad (1)$$

$$\sigma_{strut} = \frac{\sigma_{micro-lattice} \cdot 3L^3}{4\sqrt{2}d^3} \quad (2)$$

Table 2 Comparison of micro-strut properties derived from micro-lattice block compression test and individual strut tensile test with standard properties.

Ti-6Al-4V Properties	**Young's Modulus, E**	**Ultimate stress, σ**
From tensile test	45 MPa	280 MPa
From compression test	101 GPa	521 MPa
Standard properties [7]	114 GPa	950 MPa

The derived properties of the single strut using the micro-lattice block properties were tabulated in Table 2 and compared with that of standard properties [7] as well as properties of strut determined from tensile test. The results show that the strut properties derived from the micro-lattice blocks are comparable to that of standard properties values, with Young's Modulus value of 89% and ultimate stress value of 55% from the standard values. However, these comparisons need to be fully analyzed using different parameters that involve in the manufacturing of micro-lattice, yet the optimization works need to be done.

4. SUMMARY

The basic unit in a micro-lattice structure which is the strut is an important part to be characterized. The manufacturing route and geometry of the basic unit contribute to the deformation and failure of that individual part, and this affect the failure prediction of a structure. The result from this study shows that the strut properties can be derived from the micro-lattice block structure by using theoretical equation and the values are comparable to that of standard properties, but yet need to be optimized.

5. ACKNOWLEDGEMENT

R. Hasan gratefully acknowledges The Ministry of Higher Education, Malaysia and Universiti Teknikal Malaysia Melaka (UTeM) for the scholarship and financial support, as well as the University of Liverpool for the opportunity to do the research.

REFERENCES

[1] R. Mines, Y. Girard, V. Fascio, "On the development of conventional and micro lattice cellular metals as core materials in aerospace sandwich construction", in *Proceedings of the International European SAMPE,* Europe, 2009, pp. 248-256.

[2] O. Rehme, *Cellular Design for Laser Freeform Fabrication*, Gottingen: Cuvillier Verlag; 2010.

[3] H. Hooputra, H. Gese, H. Dell, H. Werner, "A comprehensive failure model for crashworthiness simulation of aluminium extrusions", *International Journal of Crashworthiness*, vol. 9, no. 5, pp. 449-463, 2004.

[4] R. Hasan, Progressive collapse of titanium alloy micro-lattice structures manufactured using selective laser melting, United Kingdom: University of Liverpool; 2013.

[5] R. Hasan, R.A.W. Mines, S. Tsopanos, "Determination of elastic modulus value for selectively laser melted titanium alloy micro strut," *Journal of Mechanical Engineering Technology*, vol. 2, no. 2, pp. 17-25, 2010.

[6] R. Hasan & R.A.W Mines, "Variations in diameter of struts for micro-lattice structure manufactured using selective laser melting", in *Proceedings of Mechanical Engineering Research Day, 2016*, pp. 119-120.

[7] R. Boyer, G. Welsch, E.W. Collings (ed.), *Material Properties Handbook: Titanium Alloys*, Material Park, OH: ASM International; 1994.

[8] K. Ushijima, W.J. Cantwell, R.A.W. Mines, S. Tsopanos, M. Smith, "An investigation into the compressive properties of stainless steel micro-lattice structures", *Journal of Sandwich Structures and Materials*, vol. 13, pp. 303-329, 2011.

Heat Sensitivity on ASTM A36 mild steel plate joint using low energy arc joining welding

Saiful Din Sabdin*, Nur Izan Syahriah Hussein, Mohammad Kamil Sued, Mohamad Nizam Ayof

Faculty of Manufacturing Engineering, Universiti Teknikal Malaysia Melaka, Hang Tuah Jaya, 76100 Durian Tunggal, Melaka, Malaysia

*Corresponding e-mail: saifulkdh@yahoo.com

Keywords: Thin plate; arc welding; steel; heat input

ABSTRACT – Low energy arc joining in GMAW have been perfected to provide the welder with greater control over the arc and heat input to allow for the wire welding of thin or sensitive joints to be performed. The main objectives this experiment to identified parameter that conductive heat transfer dominates other effects in ASTM A36 mild steel using ColdArc machine, which causes the differences in sensitivity of the process to the input parameters (current and voltage). The study of this paper covers only the effects of varying heat input on the voltage and current responses of the weldment after cooling down to room temperature.

1. INTRODUCTION

Heat sensitivity is one of the most important process parameters in controlling weld response [1]. It can be referred to as an electrical energy supplied by the welding arc to the weldment. In order to protect the quality and the cost, the use of light material has become an interest among industries. A new variation on conventional short-circuit arc welding introduces changes to the electric current. The course of the arc's voltage in the coldArc welding method is identical to the traditional short-circuit arcs, with only principle difference occurring in the course of its electric current.

Thin plate can defined as the plate's transverse dimension, or thickness, is small compared to the length and width dimensions [2] . Analysis of welded products in industry shows an important share of welding thin sheet metal. During welding, temperature variations in welds and parent metals have important effects on material characteristics, residual stresses as well as on dimensional and shape accuracy of welded products. This is especially important in the case of thin sheet metal products, where control over welding distortions or deformations is difficult. One of the purposes of the development in thin plate welding technology is to investigated parameter current and voltage for ColdArc machine.

The ColdArc process is considered as a prospective welding process for sheet metal industry with narrow fabrication tolerances, higher demands for the quality of the product as well as its productivity. To improve the quality, flexibility and productivity of the welding performance and the process of automatization using welding robots is important. Therefore, the heat input can cause problems of distortion and residual stresses are always of great concern in welding industry. In order to deal with this problem, it is necessary to define prediction of the amount of heat input resulting from the welding operations.

2. METHODOLOGY

The experiments were conducted according to the information obtained from literature [3-4] and using the welding parameters given in [5]. Selection of current and voltage parameters are randomly based on experimental observations in this paper. The robot welding used in this study was KUKA type KRC4 with the system is equipped EWM ColdArc power source. Specimens dimension of 250 mm × 50 mm were fabricated. In order to reduce the test program, one specimen was used in welding of three welds with different welding parameters.

Welding experiments were conducted with similar materials i.e. plate with ASTM A36 (mild steel). The thickness of the materials was 1 mm with welds was performed on lap joint. Solid welding wires grades ER70S-6 for mild steel with diameter 1.0 mm and gas mixture 70 % Argon + 30 % CO2 was employed in the process.

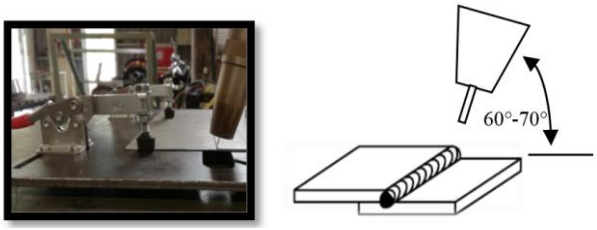

Figure 1 Lap joint.

3. RESULTS AND DISCUSSION

Effect of heat input can approximately (i.e., if the arc efficiency is not taken into consideration) be characterized as the ratio of the arc power supplied to the electrode to the arc travel speed, as shown in the following equation:

$$Q = V \times I \times \frac{60}{v} \quad (1)$$

Table 1 outlines the preliminary experimental result. Visual examination showed that unequal curvature and angle of the welding joints occurred. According to ISO 5817 of the standard for welding quality, welded joints can be classified according to uniform and regular joint. Lap joints were produced without welding sparks. In this

experiment determined parameter values for pre flow time and post flow time flow time of 0.1 seconds. While the wire speed is set at 2.5 m / min and welding speed of 0.6 m / min. Parameter changes done on the current and voltage.

The effects of varying heat input on the thin plate is illustrated in Figure 3 and 4 Obviously, the results showed that the welding heat input has significant effect on the welding responses by current and voltage. When heat input increase when variable parameter increase. Welding the mild steel with thickness of 0.5–1 mm, the heat input was in the range of 0.130–0.133 kJ/mm. For mild steel, further studies are to be conducted to determine the heat input parameters. The results obtained in this study correlate with the results obtained in [6], where the ColdArc technology was adopted for welding the similar metals. Excessive concavity was noted, also it depends on the welding speed and current. The ColdArc process proves to be suitable for welding thin sheet metal. It is essential to determine the right welding speed (speed range) to guarantee low porosity and to minimize distortions in the product. Using the above mentioned welding method and welding speed in the 0.6 m/min for welding mild steel proved to be the most appropriate.

Table 1 Preliminary experimental result.

No	Parameter	No. of Sample				
		1	2	3	4	5
1	Welding speed (m/min)	0.6	0.6	0.6	0.6	0.6
2	Ampere(A)	70	75	77	78	95
	Voltage (v)	7.5	16.8	17	17	17.6
4	Wire speed (m/min)	2.5	2.5	2.5	2.5	2.5
5	Pre flow time (s)	0.1	0.1	0.1	0.1	0.1
6.	Post flow time (s)	0.1	0.1	0.1	0.1	0.1
Visual ISO 5817 (result)		√	√	√	√	√

4. CONCLUSIONS

The most significant findings from this study is that output responses are related to heat sensitivity on ASTM A36 mild steel joint. After completion of this work, several conclusions are made from the results shown above. Based on the preliminary results i.e. results shown above in figures we can predict the heat input and distortion of weldment numerically. This is cost saving process because experimental processes are costly. From the results we also conclude that heat input, welding speed has significant impacts on the weld response which are as follows:

a) The experiments shown that these methods successfully applied to welding ASTM A36 (mild steel) with thicknesses of 1 mm. It is worth noting that these methods allow creating lap joints of thin sheets, even with a thickness of 1 mm, which was hitherto impossible using traditional welding equipment for welding with consumable electrodes in gas shielding, and MIG welding of such materials caused great difficulty.

b) When current and voltage increase the heat input increase.

c) Visual inspection shows good result when constantly welding speed, pre flow, and post flow time and wire speed.

d) Increasing the preflow and optima, post floest flow time robot welding to 0.15s can cause holes.

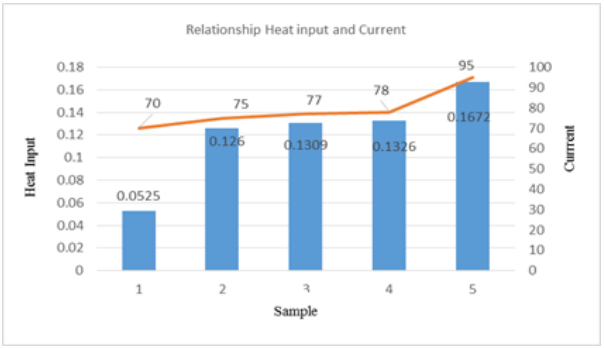

Figure 3 Relationship heat input and current.

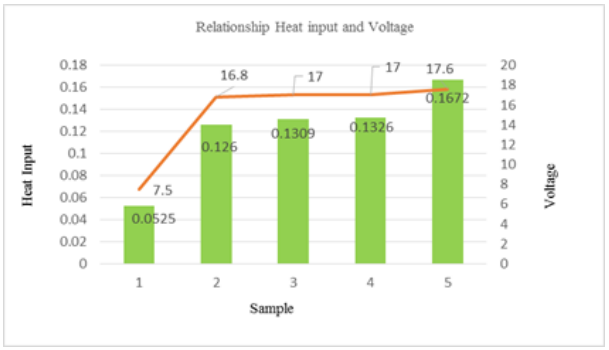

Figure 4 Relationship heat input and voltage.

ACKNOWLEDGEMENT

The authors would like to thank the Faculty of Manufacturing Engineering, Universiti Teknikal Malaysia Melaka (UTeM) and Advanced Technology Training Center (ADTEC) Batu Pahat for educational and technical support throughout this research.

REFERENCES

[1] M.H.K. Chavan and D.M.S. Kadam, G.D. Shelake, "Effect of heat input and speed of welding on Distortion," *Int. J. Ind. Eng. Res. Dev.*, vol. 3, no. 2, pp. 42–50, 2012.

[2] C.R. Steele and C.D. Balch, "Introduction to the Theory of Plates Stretching and Bending of Plates - Fundamentals," pp. 1–41.

[3] P. Taylor and M. De Dompablo, "New solutions in coldArc and forceArc welding technology," *Weld. Int.*, vol. 27, no. December 2014, pp. 37–41, 2013.

[4] P. Kah and J. Martikainen, "Current Trends In welding Processes And Materials : Improve In effectiveness," *Rev. Adv. Mater. Sci.*, vol. 30, pp. 189–200, 2012.

[5] P. Miguel, S. Almeida, and N. Titanium, "Innovations in arc welding," *5º Congr. Luso-Moçambicano Eng.*, no. April 2016, 2011.

[6] P. Kah, R. Suoranta, and J. Martikainen, "Advanced gas metal arc welding processes," 2012.

Effect of ZnO composition on the surface morphology and frictional properties of electrodeposited nickel-fly ash composite coating

Muhamad Khaizaki Ahmad, Intan Sharhida Othman*, Muhammad Zaimi Zainal Abidin, Noraiham Mohamad, Rose Farahiyan Munawar, Emmy Nurulazwana Azhar

Carbon Research Technology Research Group, Advanced Manufacturing Centre, Faculty of Manufacturing Engineering, Universiti Teknikal Malaysia Melaka, Hang Tuah Jaya, 76100 Durian Tunggal, Melaka, Malaysia

*Corresponding e-mail: intan_sharhida@utem.edu.my

Keywords: Ni-fly ash; composite coating; zinc oxide

ABSTRACT – The nickel-fly ash (Ni-FA) composite coatings were deposited on aluminium alloy 7075 (AA7075) substrate by using electrodeposition technique. Prior to electrodeposition of Ni coating on AA7075, a zincating pre-treatment process is needed to activate the substrates surface. The composition of ZnO in zincating solution was varied. The electrodeposition process was carried out for 1 hour at 40°C under the current density of 3 A/dm^2 in a modified nickel Watt's bath containing FA particles. The produced composite coatings were characterized and tested using scanning electron microscopy and wear tester. As composition of ZnO increased, surface morphology of Ni-FA composite coating becomes finer. The coefficient of friction of the coating decreses as the composition of ZnO increased.

1. INTRODUCTION

Aluminium alloy 7075 (AA7075) are widely used in marine, automotive and aerospace industry due to its superior strength to weight ratio compared to other aluminium alloy series [1-2]. However, due to its alloying element such as zinc, copper and magnesium, it contributes to the reduction of corrosion resistance [3]. Thus, nickel composite coating is introduced to AA7075 to improve its properties.

Prior to electrodeposition of Ni-FA composite coating on AA7075, a zincate pre-treatment is needed by immersion technique. This is due to aluminium alloy are rapidly oxidized during rinsing and/or exposed to air which resulting in adhesion failure. Zincating is an electrochemical exchange reaction which occurred between zinc complexes in the solution and the aluminium substrate. The sodium hydroxide in the zincating solution dissolved the oxide film prior to zincating which then takes place by displacement process. The zincate layer is then displaced by a nickel layer, which then becomes thickened by deposition [4].

Hence, the effect of zinc oxide (ZnO) composition in the zincating solution is still less known. Therefore, this study is aim to investigate the effect of zinc oxide composition towards Ni-FA composite coating. Thus, the characterization on the cross section and surface morphology and wear test on the Ni-FA composite coating will be investigated.

2. METHODOLOGY

The aluminium alloy 7075 (AA7075) substrate with dimension 40 mm x 30 mm x 3 mm were grind using silicon carbide papers. The substrates were first cleaned with acetone, and then followed by immersion in 10 wt. % of sodium hydroxide (NaOH) solution for 10 seconds and immersion in 50 vol. % of nitric acid (HNO_3) for 20 seconds. The zincating chemical composition and parameter were summarized in Table 1.

Table 1: Chemical composition of zincate bath and its operating condition.

Composition of Zincate Solution	**Concentration (g/L)**
Zinc oxide	40, 80, 120
Sodium hydroxide	525
Ferric chloride	1
Potassium sodium tartarate	9.8
Operating Conditions	
Temperature (°C)	RT
Time (min)	5

The chemical composition and operating condition for electrodeposition of Nickel-Fly ash (Ni-FA) composite coating on AA7075 substrate were summarized in Table 2. The cross section and surface morphology of the Ni-FA composite coating was characterized using scanning electron microscopy. The wear testing was performed using pin on-disc wear tester.

Table 2: Composition of modified nickel Watt's bath solution and its operating condition.

Composition	**Concentration (g/L)**
Nickel sulphate hexahydrate	200
Nickel chloride	20
Boric acid	30
Sodium citrate	30
Operating Conditions	
Temperature (°C)	40
Deposition time (min)	60
Current density (A/dm^2)	3
Composition of FA (g/L)	25

3. RESULTS AND DISCUSSION

In Figure 1, the cross section of the Ni-FA composite coatings produced from various ZnO composition were shown. The average thickness of the

composite coatings is 53.97 µm. A non-uniform nickel deposit was observed at the interface of the coating and substrate of a sample which was produced from the lowest composition of ZnO (40 g/L), as shown by Figure 1(a). The figure also shows a formation of cavities at the interface of coating and substrate. On the other hand, by increasing the ZnO composition to 80 and 120 g/L show a uniform interface of nickel deposits on the AA7075 substrate without any defects (Figure 1(b & c). This is due to the uniform coverage of the zinc particles on the substrate for nickel deposition, compared to 40 g/L of ZnO composition.

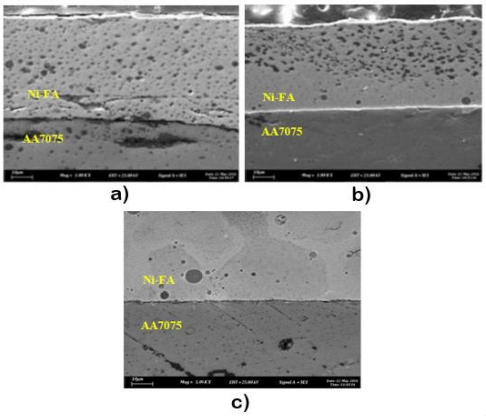

Figure 1 SEM micrograph of the cross section of coating produced at various ZnO composition (a) 40 g/L, (b) 80 g/L and (c) 120 g/L.

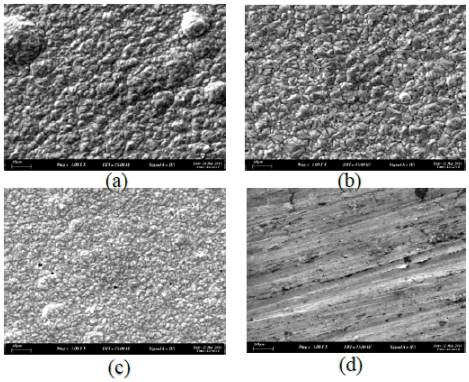

Figure 2 SEM micrographs of the surface morphology of coating produced at various ZnO composition (a) 40 g/L, (b) 80 g/L, (c) 120 g/L and bare AA7075.

Morphologies of Ni-FA composite coatings produced at various ZnO compositions are shown in Figure 2. The morphology of Ni- FA composite coating produced at 120 g/l of ZnO is more uniform and smooth (Figure 2(c), which contained refined coating structure, as compared to the coatings which produced at lower ZnO composition (Figure 2(a & b). This is due to the high density of zinc particles deposited on the substrate which act as a nuclei site for nickel growth, thus refined the nickel grain size.

The effect of ZnO composition on the coefficient of friction (CoF) of composite coatings is shown in Figure 3. It is observed that the average of CoF of Ni-FA coating is decreased as the composition of ZnO increase. Based on the data, the highest composition of ZnO can increase the wear resistance. This is due to the composition of the ZnO increased; the grain sizes are refined and make the contact layer surface move smoothly. Thus, the decreasing of the coefficient of friction exhibit the coating has better wear resistance.

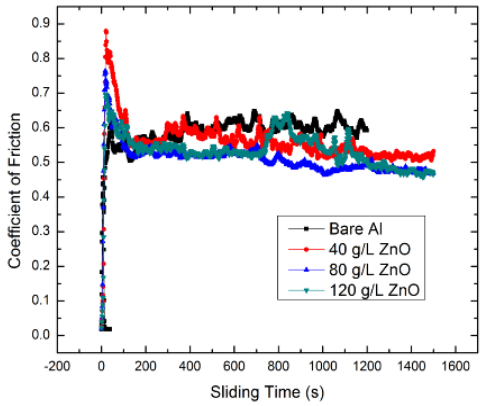

Figure 3 Variation of coefficient of friction of the coatings with sliding time.

4. CONCLUSION

From the experiment investigation given, the following important deductions could be made:

a) As composition of ZnO increased, it shows the Ni deposited on AA7075 substrate produce more smooth and uniform interface without any defect.
b) The morphology of Ni-FA composite coating produce more refined coating structure at higher composition of ZnO.
c) The coefficient of friction decrease as the composition of ZnO increased. Thus, indicate the coating produce have better wear resistance.

ACKNOWLEDGEMENTS

Grant no.: RAGS/1/2014/TK04/FKP/B00074

REFERENCES

[1] E.S. Puchi-Cabrera, C. Villalobos-Gutierrez, I. Irausquin, J. La Barbara-Sosa and G. Mesmacque, "Fatigue behavior of a 7075-T6 aluminium alloy coated with an electroless Ni-P deposit," *International Journal of Fatigue*, vol. 28, no. 12, pp. 1854-1866, 2006.

[2] I. Irausquı, J. La Barbera-Sosa and G. Mesmacque, "Fatigue behavior of a 7075-T6 aluminum alloy coated with an electroless Ni–P deposit," *International Journal of Fatigue*, vol. 28, pp. 1854-1866, 2006.

[3] S.M. Kumar, R. Pramod, M.S. Kumar and H.K. Govindaraju, "Evaluation of fracture toughness and mechanical properties of aluminum alloy 7075 T6 with nickel coating," *Procedia Engineering*, vol. 97, pp. 178–185, 2014.

[4] C.F. Oduoza and E. Khan, "Nickel-phosphorus deposition on pretreated aluminium alloys during immersion in electroless nickel bath," Mater. Sci. Eng., vol. 1, pp. 457–471, 2011.

Fabrication and characterization of carbon nanofibres from polyacrylonitrile precursor

N.A. Munajat[1], A.H. Nurfaizey[1,2,*], S.H.S.M. Fadzullah[1,2], G. Omar[1,2], J. Jaafar[3], N.S.A. Roslan[3], M.H.M. Husin[3]

[1)] Faculty of Mechanical Engineering, Universiti Teknikal Malaysia Melaka,
Hang Tuah Jaya, 76100 Durian Tunggal, Melaka, Malaysia
[2)] Centre for Advanced Research on Energy, Universiti Teknikal Malaysia Melaka,
Hang Tuah Jaya, 76100 Durian Tunggal, Melaka, Malaysia
[3)] Advanced Membrane Technology Research Centre (AMTEC),
Universiti Teknologi Malaysia, 81310 UTM Johor Bahru, Johor, Malaysia

[*]Corresponding e-mail: nurfaizey@utem.edu.my

Keywords: Electrospinning, electrospun nanofibre, carbon nanofibre, polyacrylonitrile

ABSTRACT – This study is about fabrication and characterization of polyacrylonitrile (PAN) based electrospun carbon nanofibres using electrospinning technique. PAN precursor solution was prepared by dissolving PAN pellets into N,N-Dimethylformamide (DMF). The electrospun nanofibers were stabilized at 240ºC and later carbonized at 800ºC in a nitrogen filled furnace. The characterization of the nanofibres was carried out using ATR-FTIR, SEM, and Image J Software. PAN based carbon nanofibres have been successfully fabricated and characterized. This conductive carbon based nanofibre material is highly potential for sensor applications.

1. INTRODUCTION

Electrospinning is well known as the most versatile and economical method for producing polymeric nanofibres [1]. The auspicious characteristic of nanoscale fibre size is advantageous for numerous applications such as sensors, smart materials, filtrations, fuel cells and drug delivery [2]. A typical electrospinning setup consists of a polymer solution supply which flows through a spinneret, a high voltage power source, and a grounded collector as shown in Figure 1. The presents of high strength electric field in spinneret tip has overcome the surface tension of the droplet cause a stream or jet is ejected from the droplet and it is called as nanofiber [3].

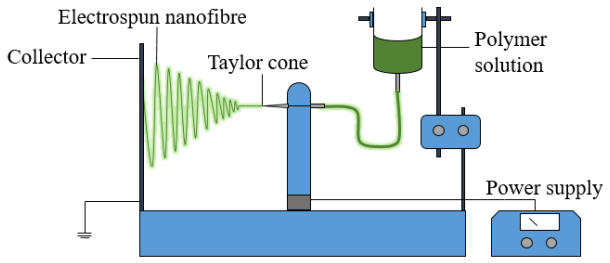

Figure 1 A schematic diagram of a typical electrospinning setup.

Nowadays, there are increasing concerns on toxicological impact and possible hazard of free nanoparticles to human health and the environment [4]. There is a need for simple and effective detection and monitoring devices suitable for sensing these particles. This is because, the nano size particle tends to stick to the surface of nanofiber by the present of electrostatic and London-Van Der Waals forces [5]. In this regard, a membrane made of conductive electrospun nanofibres is potential to be used as replacement materials. The aim of this study is to fabricate and characterize PAN based carbon nanofibres for sensor applications.

2. METHODOLOGY

Polyacrylonitrile (PAN) electrospun nanofibre was produced using Electrospinz Model ES1a (Electrospinz Ltd., NZ). The PAN polymer solution was prepared by dissolving 10 wt% of PAN into N,N-Dimethylformamide (DMF) and stirred for 24 hours at room temperature using a magnetic stirrer model C-MAG HS7 (Ika Works, Malaysia). The PAN polymer has an average molecular weight of 124,000-130,000 g/mol (Sigma Aldrich). Throughout electrospinning process, the voltage was set at 10 kV whilst the distance between the spinneret to collector was set at 20 cm. Stabilization of the nanofibres was carried out at 240ºC for about 1 hour using an oven. Carbonization of the fibres was carried out by heating the fibres at 800ºC for about 1 hour in a nitrogen filled gas furnace. The change of functional group after pyrolysis process was examined using a Fourier Transform Infrared (FTIR) PerkinElmer Spectrum 100 FTIR spectrometer (USA). Scanning electron microscope (SEM) Model JSM-5010PLUS/LV (Jeol Ltd., Japan) was used to examine the morphology of the fibres and ImageJ version 1.50 software (National Institutes of Health, USA) was used to analyze the SEM micrographs.

3. RESULTS AND DISCUSSION

The as-spun PAN nanofibres originally appeared white in appearance but then turned brown after stabilization process at 240ºC (Figure 2). After carbonization process (pyrolysis) at 800ºC, the fibres appeared black indicating that decomposition of other organic compounds has taken place.

The peak intensity at 2244 cm^{-1} was dramatically reduced after the stabilization process at 240ºC (Figure 3). This is because fully aromatized-cyclized-ladder structures were formed through the nitrile group reaction

in cyclization process. However, this PAN nanofibres were not fully stabilized because of the presence of small peaks as can be observed at the peak intensity of 2244 cm^{-1}. These small peaks could be eliminated by increasing the stabilization temperature to about 280 ^oC. During carbonization, these peaks were eliminated after pyrolysed at 800 ^oC. However, the full conversion of polymer to carbon was not achieved due to the existence of other compounds [6] as the aliphatic CH groups at peak intensity of 1540 cm^{-1} were still visible after the carbonization process. This could be caused by insufficient heat used during the carbonization and further works are ongoing to verify this claim.

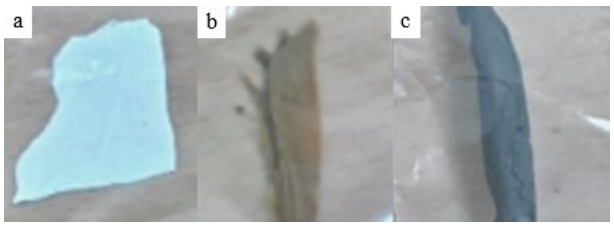

Figure 2 Visual appearance of (a) PAN nanofibres (b) stabilized nanofibres and (c) carbonized nanofibers.

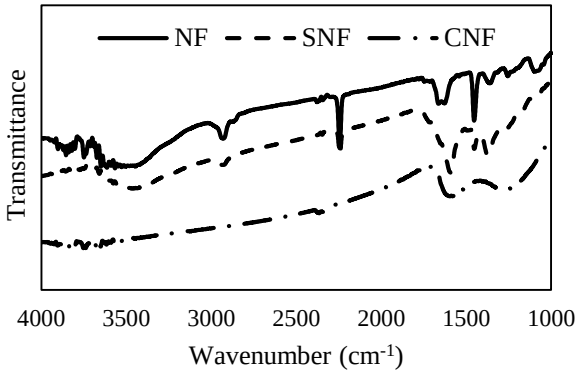

Figure 3 FTIR spectra of PAN nanofibers (NF), stabilized nanofibers (SNF), and carbonized nanofibers (CNF).

As it can be clearly observed from SEM micrographs, solid electrospun nanofibres were produced from electrospinning process (Figure 4). As expected, the fibres diameter reduced after each stabilization and carbonization process. The average diameter of the fibres for as-spun PAN, stabilized, and carbonized nanofibres were 1028.59 nm, 611.67 nm, and 303.44 nm respectively.

Combination of small fibre size and good conductivity of carbon based materials makes PAN based carbon nanofibre a potential material for sensor applications. Further investigation on the physical and electrical properties of this PAN based carbon nanofibres are ongoing and the results will be reported elsewhere.

4. CONCLUSION

In this study, carbon nanofibres were successfully fabricated from PAN precursor using electrospinning technique. FTIR results showed the conversion of polymer to carbon by removal of other compounds through thermochemical decomposition. The fibre diameter of nanofibres was significantly reduced after heat treatment. This nanoscale carbon based material is highly potential to be used for sensor applications.

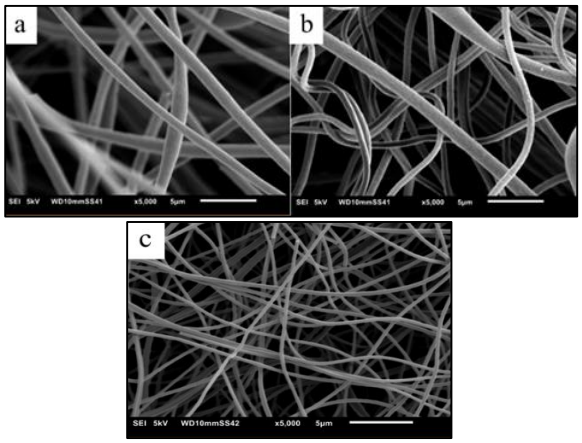

Figure 4 Scanning electron micrographs of (a) as-spun PAN nanofibres (b) stabilized nanofibres and (c) carbonized nanofibers.

ACKNOWLEDGEMENT

Grant no.: PJP/2016/FKM/HI1/S01466. Special thanks to the members of Advanced Materials Research Group (A-MAT), Advanced Membrane Technology Research Centre (AMTEC), UTM and the members of the Faculty of Mechanical Engineering, UTeM.

REFERENCES

[1] [P. Ramesh Kumar, N. Khan, S. Vivekanandhan, N. Satyanarayana, A.K. Mohanty and M. Misra, "Nanofibers: Effective generation by electrospinning and their applications," *J. Nanosci. Nanotechnol.*, vol. 12, no. 1, pp. 1–25, 2012.

[2] N. Kaur, V. Kumar and S.R. Dhakate, "Synthesis and characterization of multiwalled CNT – PAN based composite carbon nanofibers via electrospinning," *Springerplus*, 2016.

[3] A.H. Nurfaizey, J. Stanger, N. Tucker, N. Buunk, A.R. Wood, M.P. Staiger and N.T. Nicktucker, "Control of Spatial deposition of electrospun fiber using electric field manipulation," *J. Eng. Fiber. Fabr.*, vol. 9, no. 1, pp. 155–164, 2014.

[4] C. Buzea, I.I. P. Blandino and K. Robbie, "Nanomaterials and nanoparticles : Sources and toxicity," *Biointerphases*, vol. 2, no. 4, pp. 1–103, 2007.

[5] A.H. Nurfaizey, N. Tucker, J. Stranger, and M.P. Staiger, "Functional nanofibers in clothing for protection against chemical and biological hazards," Woodhead Publishing, pp. 62–86, 2012.

[6] F. E. C. Othman, N. Yusof, J. Jaafar, A.F. Ismail, H. Hasbullah, N. Abdullah and M.S. Ismail, "Preparation and characterization of polyacrylonitrile/ manganese dioxides- based carbon nanofibers via electrospinning process," *IOP Conf. Ser. Earth Environ. Sci.*, vol. 36, p. 12006, 2016.

Parametric study of low-field magnetic resonance imaging of articular cartilage in synovial joint

M.J. Abd. Latif[1,2,*], R. Seeni Ibramsa[1], N.H. Mohd. Saad[2,3]

[1)] Faculty of Mechanical Engineering, Universiti Teknikal Malaysia Melaka, Hang Tuah Jaya, 76100 Durian Tunggal, Melaka, Malaysia
[2)] Centre for Robotics & Industrial Automation, Universiti Teknikal Malaysia Melaka, Hang Tuah Jaya, 76100 Durian Tunggal, Melaka, Malaysia
[3)] Faculty of Electronics and Computer Engineering, Universiti Teknikal Malaysia Melaka, Hang Tuah Jaya, 76100 Durian Tunggal, Melaka, Malaysia

[*]Corresponding e-mail: juzaila@utem.edu.my

Keywords: Low-Field MRI; MRI Sequence; articular cartilage

ABSTRACT – Low-field Magnetic Resonance Imaging (MRI) had been utilized to measure the geometrical data of the living tissues such as thickness and volume. However, various imaging parameters were used to image the articular cartilage tissue. Therefore, the aim of this study was to investigate the imaging parameters of low-field MRI in order to produce good quality image of cartilage tissue. Five different imaging sequences were used to scan the articular cartilage of bovine hip joint. The images were visually compared to examine the best sequence which could provide good image of cartilage. The gradient echo and spin echo T1 demonstrated the potential imaging sequence of low-field MRI system that could provide sufficient image quality of cartilage tissue.

1. INTRODUCTION

Cartilaginous tissues are extensively distributed in human joint anatomy because of its importance to the body movement. The human physical demand expose the cartilage tissue to degeneration and may leads to osteoarthritis disease which restricts body movement [1].

MRI has become essential diagnosis procedure to monitor the condition of articular cartilage since it was introduced to medical imaging in early 1970s [2]. High-field MRI techniques have successfully been developed to provide measures of the macromolecular environment within cartilage tissue [3-4]. This is possible via the interaction between interstitial water, probed by MRI, and the macromolecular constituents that affect the nuclear magnetic relaxation properties characterizing the spin energetics of the water proton system [5].

Recently, imaging on low-field strength (<0.5T) has gained increasing popularity due to its smaller size, lower initial purchase price compared to high-field MRI, lower operational costs, and easily installed scanners [6]. It also shows the potential of producing similar image quality of high-field MRI [7]. Therefore, this study aimed to investigate the image parameters of low-field MRI system in order to obtain good quality image of cartilage tissue.

2. METHODOLOGY

2.1 Sample preparation

Bovine hip joint was obtained within 24 hours after slaughter from local abattoir. Excess ligaments and flesh of the joint were discarded as shown in Figure 1. The specimen was kept in moist condition prior scanning.

Figure 1 Bovine hip joint.

2.2 Low-field magnetic resonance imaging

The joint was imaged using 0.18 T low-field MRI system (Esaote C-Scanner, Genova, Italy). The hip joint was positioned in in the middle of the MRI coil with the lower hip bone was at 180° flexion. Five imaging sequences were used which were the gradient echo (GE), gradient echo short-T1 inversion recovery (GE-STIR), spin echo T1 (SE-T1), spin echo T2 (SE-T2) and turbo spin echo (Turbo SE). The parameters of the imaging sequences are tabulated in Table 1.

3. RESULTS AND DISCUSSION

The articular cartilage images from five different imaging sequences of the low-field MRI are shown in Figure 2. Visually GE and SE-T1 shows better image quality compared to other sequences.

GE and SE-T1 sequences were also used in other low-field MRI systems to image the articular cartilage due to the better definition of the anatomic structure of the synovial joint and maximizes the signal and contrast between the joint structures [8-9].

Table 1 Imaging parameters of different sequences.

Parameters	Sequences				
	GE	GE STIR	SE T1	SE T2	Turbo SE
TE (ms)	18	16	26	90	90
TR (ms)	1400	2760	1520	4940	4940
Slices No.	31	31	31	31	31
FOV (mm)	180	180	180	180	180
Matrix	256	256	256	256	256
Thickness (mm)	4	4	4	4	4

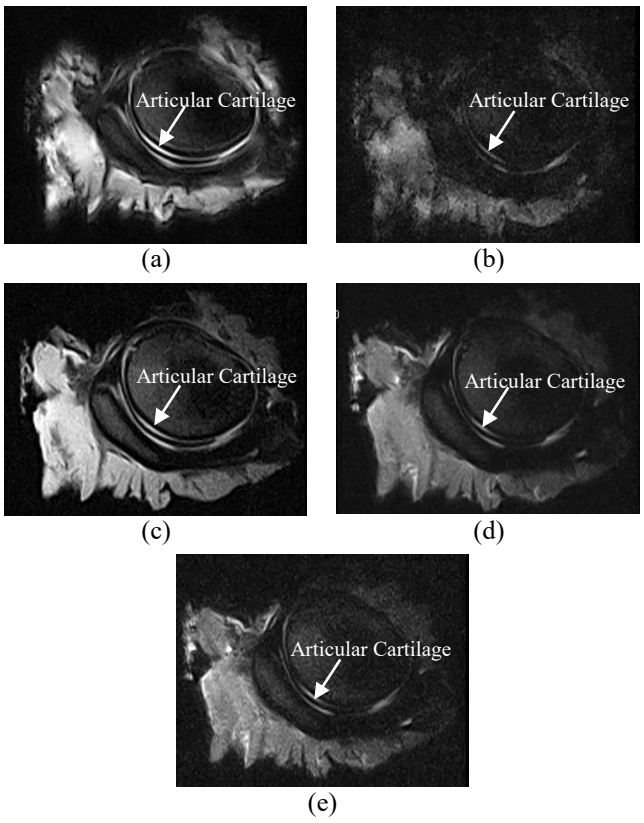

Figure 2 Articular cartilage MRI images from different imaging sequences; (a) GE, (b) GE-STIR, (c) SE-T1, (d) SE-T2, and (e) Turbo SE

Cartilage grayscale intensity analysis of these two sequences shows different range of values for the same image region of interest (ROI). Grayscale average for GE is 1016.52±525.88 and SE-T1 is 991.69±479.96. Based on the standard deviation, GE could provide better grayscale range of the articular cartilage.

However, due to hyper-intense effect on the images produced using GE sequence [9], the images are needed to be interpreted with caution because it may demonstrate a high number of artifacts. Thus, SE-T1 becomes the final selected sequence to be considered for further study.

4. CONCLUSION

Based on the results, it was found that the SE-T1 is the suitable sequence that can produce good quality image of cartilage tissue compared with other sequences that are available in low-field MRI system. This imaging sequence could be used for further studies to monitor the condition of the cartilage tissue in synovial joint.

ACKNOWLEDGEMENTS

This work was supported by Universiti Teknikal Malaysia Melaka (UTeM) and financially supported by the Ministry of Higher Education (MOHE) Malaysia under Fundamental Research Grant Scheme (FRGS/ 1/2015/TK05/FKM/02/F00272) is acknowledged.

REFERENCES

[1] W.D. Blackburn, S. Chivers and W. Bernreuter, “Cartilage imaging in osteoarthritis,” *Semin. Arthritis Rheum.*, vol. 25, no. 4, pp. 273–281, 1996.

[2] C.S. Winalski and P. Rajiah, “The evolution of articular cartilage imaging and its impact on clinical practice,” *Skeletal Radiol.*, vol. 40, no. 9, pp. 1197–1222, 2011.

[3] K. Rathnayaka, K.I. Momot, A. Coulthard, A. Volp, T. Sahama, M. A. Schütz and B. Schmutz, “Anatomical MR imaging of long bones: comparative performance of MRI at 1.5 T and 3 T,” *Biomed. Spectrosc. Imaging*, vol. 2, no. 1, pp. 21–35, 2013.

[4] M.C. Chou, P.H. Tsai, G.S. Huang, H.S. Lee, C.H. Lee, M.H. Lin, C.Y. Lin and H.W. Chung, “Correlation between the MR T2 vlue at 4.7 T and relative water content in articular cartilage in experimental osteoarthritis induced by ACL transection,” *Osteoarthr. Cartil.*, vol. 17, no. 4, pp. 441–447, 2009.

[5] S. Shen, H. Wang, J. Zhang, F. Wang and M. Chen, “T1ρ Magnetic Resonance imaging quantification of early articular cartilage degeneration in a rabbit model,” *BMC Musculoskelet. Disord.*, vol. 16, no. 1, p. 361, 2015.

[6] B.J. Ejbjerg, E. Narvestad, S. Jacobsen, H. S. Thomsen, and M. Østergaard, “Optimised, low cost, low field dedicated extremity MRI is highly specific and sensitive for synovitis and bone erosions in rheumatoid arthritis wrist and finger joints: comparison with conventional high field MRI and radiography.,” *Ann. Rheum. Dis.*, vol. 64, no. 9, pp. 1280–1287, 2005.

[7] A. Cotten, E. Delfaut, X. Demondion, F. Lapegue, M. Boukhelifa, N. Boutry, P. Chastanet and F. Gougeon, “MR imaging of the knee at 0.2 and 1.5T: Correlation with surgery,” *Am. J. Roentgenol.*, vol. 174, no. April, pp. 1093–1097, 2000.

[8] A. Arencibia, M. Encinoso, J.R. Jáber, D. Morales, D. Blanco, A. Artiles and J.M. Vázquez, “Magnetic resonance imaging study in a normal bengal tiger (panthera tigris) stifle joint,” *BMC Vet. Res.*, vol. 11, no. 1, pp. 184–192, 2015.

[9] E. Pujol, H. Van Bree, L. Cauzinille, C. Poncet, I. Gielen and B. Bouvy, “Anatomic study of the canine stifle using low-field magnetic Resonance imaging (MRI) and MRI arthrography,” *Vet. Surg.*, vol. 40, no. 4, pp. 395–401, 2011.

Effect of weight ratios in backing material on lamb wave excitation in PZT transducers

H.S. Ilham[1,] M.N. Salim [1,2,*], A.F. Ab Ghani[1,2]

[1)] Faculty of Mechanical Engineering, Universiti Teknikal Malaysia Melaka, Hang Tuah Jaya, 76100 Durian Tunggal, Melaka, Malaysia
[2)] Centre for Advanced Research on Energy, Universiti Teknikal Malaysia Melaka, Hang Tuah Jaya, 76100 Durian Tunggal, Melaka, Malaysia

[*]Corresponding e-mail: norsalim@utem.edu.my

Keywords: Lab Wave; backing material; PZT transducer

ABSTRACT – Lamb wave inspection in aluminum plate with 4 mm depth of defect is conducted using PZT transducers with different compositions of tungsten-epoxy backing layers. Tungsten powder at ratios of 50% to 70% in weight are used to study effect of the tungsten-epoxy backing layers on the measured ringing wave from angle beam transducers. The results show significant reduction of ringing waves as well as initial waves and defect echoes in measurement when the percentage of tungsten material increased to up 70 % in weight ratio.

1. INTRODUCTION

Guided wave inspection is one of non-destructive testing (NDT) and material evaluation (NDE) techniques. The wave which propagates in plate-like structures known as Lamb wave has ability to locate defects on large structures such as storage tanks and pressure vessels in the petrochemical industries. In general applications, a suitable wave mode and frequency range are selected in order to have good sensitivity on the defect screening over the entire structures [1]. The needs on selection of wave modes and frequency range indicate the need of different PZT transducers for a specific inspection on plates with different thicknesses [2]. Moreover, instead of lacking local expertise, the cost of PZT transducers for guided wave structure health monitoring are still expensive and in some applications a number of transducers are required due to the large size of oil storage tanks and different thicknesses of the structures [3]. Thus, we studied the fundamental PZT transducer design and investigate the effect of backing material on reduction of ringing wave and at the same time it provides a good sensitivity in the PZT transducer for excitation or measurement of fundamental symmetric Lamb mode denoted as S0 mode in the next sections.

2. METHODOLOGY

Figure 1 illustrates our developed system for the excitation and measurement of Lamb wave studies in nondestructive applications. The system consists of a function generator, power amplifier, PZT transducers, pre-amplifier, data logger, and a host computer to synchronize the measurement. Excitation of S0 mode in an aluminum plate (500 mm × 1000 mm × 6 mm) is performed using a normal beam PZT transducer fixed at the left end of plate as in Fig. 1. Measurement of S0 dominant mode is made using an angle beam transducer consists of a transducer shoe and the develop transducer in Figure 2. Figure 2 (a) shows the designed transducer shoe which made of plexiglas with a fixed damping material in grooves and Fig. 2(b) depicted the arrangement of backing material in the aluminum case of PZT transducer which consists of 2 mm plexiglas as matching plate, active PZT composite with center of frequency at 100 kHz from Fiji Ceramic Inc, and the epoxy-tungsten backing material.

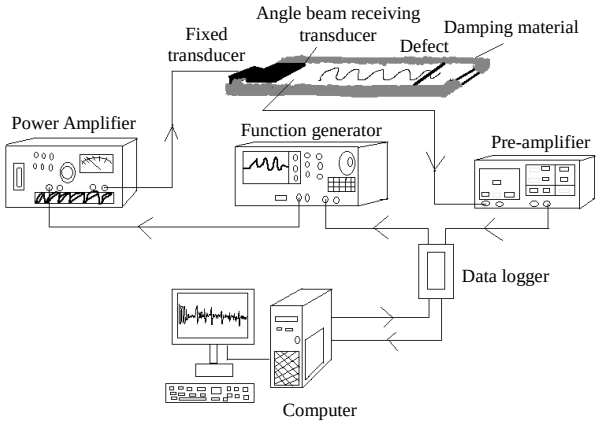

Figure 1 Excitation and measurement of S0 mode.

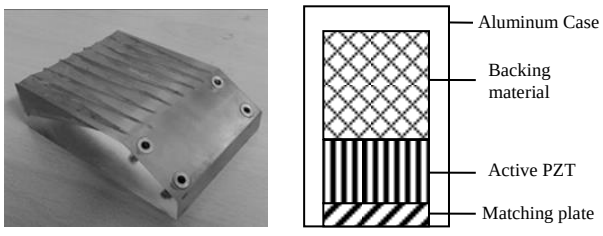

(a) Transducer shoe. (b) Backing material in transducer.

Figure 2 Transducer shoe and configuration of transducer.

Composition of tungsten-epoxy backing materials are shown in Table 1 which consist of 50% to 70% of

tungsten powder in weight ratios compared to the used epoxy material. The use of tungsten is stop at 70% in weight ratio as the further increase will cause the backing layer attenuating too much energy and give a poor sensitivity in the developed transducers.

Angle beam transducer that used to recorded the dominant S0 mode is placed on top surface at the right end of plate with groove defect at location of 800 mm from the transducers.

Table 1 Samples of tungsten-epoxy backing materials.

Percent of tungsten	Epoxy	Tungsten
50 %	15.0 g	15.0 g
60 %	14.4 g	21.6 g
70 %	12.6 g	29.4 g

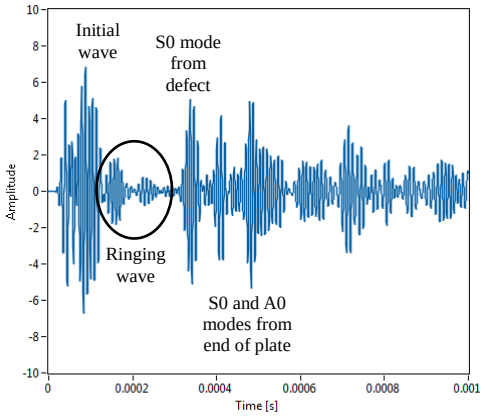

(a) 50%

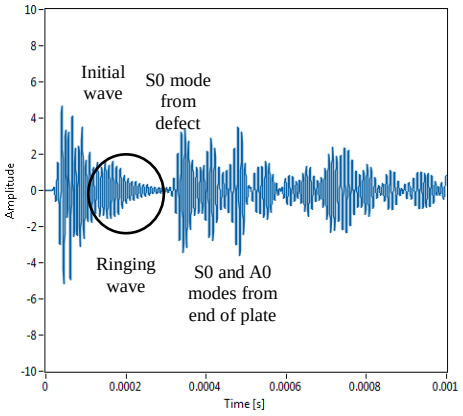

(b) 60%

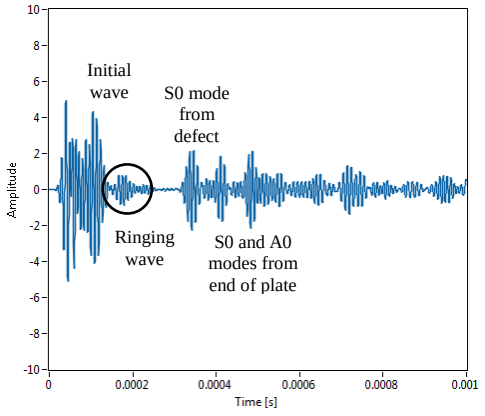

(c) 70%

Figure 3 Measured waveform from different ratios of tungsten-epoxy backing materials.

3. RESULTS AND DISCUSSION

The recorded waveforms in experiments are shown in Figure 3 for the compositions of tungsten from 50% to 70% in weight ratios.

Figure 3(a) shows measurement of S0 mode with 50% of tungsten in backing material. The result shows large ringing wave as well as initial wave and reflected waves from defect and end of plate. The increase of tungsten into 60% in weight as in Fig. 3(b) show slightly reduction in the ringing but indicated complicated wave propagation with longer wave packet. On the other hand, the use of 70% tungsten material significantly reduce the ringing wave as in Fig. 3(c). However, the reflected waves from defect and end of plate also indicated large attenuation as we increased the ratio of tungsten material into the backing material. The increase of tungsten material in backing material is likely to dampen the acoustic vibration in the transducer which can eliminate or reduce the ringing wave but also reduce the sensitivity of the transducer.

4. CONCLUSION

From the evaluation of backing layers which consist of 50 %, 60 % and 70 % of tungsten material, the results show a decrease of wave amplitudes as the percentage of tungsten material increased and the 70 percent of tungsten in backing material depicts the best in the measurement of reflected wave from defect region. The use of tungsten-epoxy backing layer shows feasibility of developing high performance Lamb wave transducers. However, the increase of tungsten material shows attenuation on the ringing wave as well as the reflected waves and a proper design of backing layer is needed to attenuate the backward propagation wave from forming the ringing in PZT transducers.

REFERENCES

[1] H. Takahiro, M. Morimasa, I. Toshiro, K. Shoji and M.N. Salim, “Fast remaining thickness measurement using a laser source scanning technique,” *Material Transactions*, vol. 53, no. 4, pp 610-616, 2012.

[2] F. Benmeddour, S. Grondel, J. Assaad and E. Moulin, “Study of the fundamental lamb modes interaction with asymmetrical discontinuities,” *Journal of NDT&E International*, vol. 41, no. 5, pp. 330-340, 2008.

[3] M.J.S. Lowe and O. Diligent, “Low frequency reflection characteristics of A0 lamb wave from a rectangular notch in plate,” Journal of Acoustical Society of America, vol. 112, no. 6, pp. 2612-2622, 2002.

Material flow visualization in bobbin friction stir welding by analogue model

M.K. Sued[1,*], A. Tamadon[2], D. Pons[2]

[1)] Advance Manufacturing Centre, Faculty of Manufacturing Engineering, Universiti Teknikal Malaysia Melaka, Hang Tuah Jaya, 76100 Durian Tunggal, Melaka, Malaysia
[2)] Faculty of Mechanical Engineering, University of Canterbury, Christchurch 8041, New Zealand

[*]Corresponding e-mail: kamil@utem.edu.my

Keywords: Friction stir welding; bobbin tool; plasticine

ABSTRACT –There is no solid theory about the parameters of process and method of control to achieve the optimum situation in Friction Stir Welding (FSW) especially in the case of Bobbin Friction Stir Welding (BFSW). In fact, due to high mechanical loads and dynamic plastic deformation the existence of the void or tunnel as a defect in weld region is one of the challenges of the process. Performing actual weld through trial and error is costly and time consuming. Additionally, modelling using finite element software is challenging and include many assumptions in the formulation that can hide important signal. A method of using multiple layers of plasticine in different colors is used to elucidate the relationships between flow regimes and defect structure near to the real circumstances of the process. The result of the study has successfully imitated the defect and the pattern between metal and plasticine.

1. INTRODUCTION

Bobbin Friction Stir Welding (BFSW) is a solid phase joining techniques, whereby interface of the two plates is located between the shoulders of rotating tool (bobbin tool). This area is being plough through by the double shoulder tool connected by a pin for mixing the materials into a bonded structure. The success of the joint is by the generation of heat and stirring created from the friction between the rotating tool and the workpiece. The material is being plasticize during joining rather than melting and solidification as in fusion welding method. This method has been patented by TWI, United Kingdom in 1991.

Process modelling has been one of the major areas of the study. This benefitting practitioner through optimized welding without the need of trials that tend to be costly and time consuming. Modelling can be conducted either using computational or empirical. The work is challenging and difficult because of the complex content of the process. The stirring of solid material involves high plastic deformation which significantly involve interaction of many variables [1]. Therefore, most study limited to heat transfer prediction and metallurgical work [2,3]. Although some studies have conducted their multi-physics modelling, but the approaches have many assumptions that can limit the actual behaviour [4,5]. Additionally, their work focuses on a single shoulder tool known as conventional friction stir welding (CFSW). Although CFSW and BFSW is known to be similar but the process setting and variable interaction is different due to the present of bottom shoulder [6].

Therefore, in this work analogue model using plasticine is being adopted to model BFSW joint. This method has been used in predicting metal forming process such as forging and extrusion. The model produce is to visualize the complex interaction between variables that finite element methods unable to fully model.

2. METHODOLOGY

A multi- layered plasticine slab has been prepared as explained by Sudarshan et al. [7]. Each layer was rolled to approximately 1.25 mm thickness. By combining thin layers of different plasticine colors, the slab has the size of 10 mm (thickness) x 100 mm (length) x 30 mm (width) per piece and set for butt joint configuration. The tool features used in this study are threaded cylinder pin with three flats and a scroll shoulder. The size of the pin is 10 mm and the shoulder diameter is 25 mm as illustrated in Figure 1. Trials were conducted on a CNC milling machine with the rotation and feed rate of 50 RPM and 50 mm/min respectively. The slab is then carefully cut with a wire cutter to reveal the cross section.

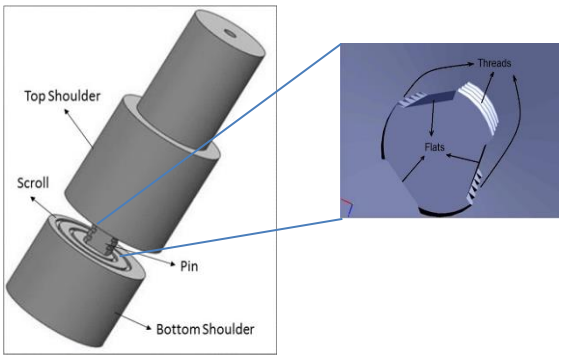

Figure 1 Bobbin tool.

The obtained cross section plasticine slab is then compared to the cross section of the actual Aluminum weld. The weld was conducted on an Aluminum Alloy 6082-T6 with a similar tool feature but having different size. The pin and shoulder diameter are 4 mm and 15 mm respectively. The welding parameters for Aluminum

were 350 RPM of rotational speed and 450 mm/min of feed rate. The reasons for different process setting is because plasticine has less yield strength in comparison with metals, therefore slower RPM and feed rate have been used.

3. RESULTS AND DISCUSSION

Figure 2 shows the cross section of the slab plasticine after the trial. By comparing this trial to the actual welding cross section in Figure 3 a similar effect is presented by the analogue model. A swivel mixing of material flow is produced at both advancing and retreating side of the slab. An interesting finding are the downward material flow at the retreating side and the upward trend of material flow at the advancing side. This analogue model finding support the suggestion by [8] whereby both downward and upward material flow present when threaded feature is used on the tool pin.

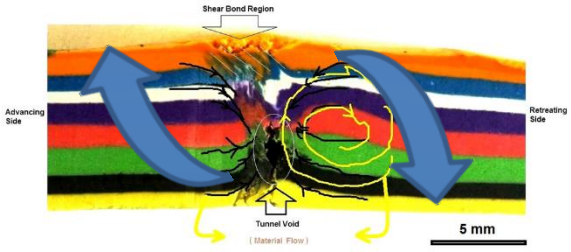

Figure 2 Analogue modeling of the Bobbin-FSW by the Plasticine slab.

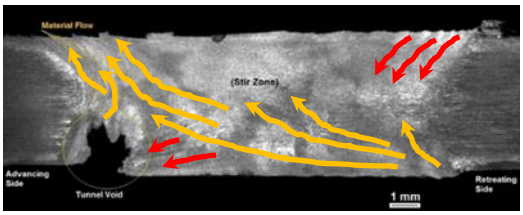

Figure 3 Weld characteristics of the Bobbin-FSW for the A6082-T6 plates.

However, a severe pulling effect is produced at the advancing side. The pull is due to the thread pitch angle which significantly impact the material present at the bottom side hence, no material mixing occurred. Material that being pushed downward at retreating side are quickly pulled upward in a slope at the advancing side. This material the being squash near the top surface because of the containment function of the shoulder.

Therefore, a tunnel or void defect present at the bottom of the advancing side and proven that this type of defect has a stronger relationship with material existent compare to the sticking and sliding mechanism which commonly due to heat generation and tool features.

4. CONCLUSION

Through the conducted research presented here, the modelling using analogue method is successfully visualized the actual impact of the FSW proses especially BFSW. Clear details of the plastic deformation mixing can be revealed. It has been shown that the pulling effect of the pin thread is present, hence causing the formation of void or tunnel at the bottom of the advancing side. This work help researcher to further understand the process and able to perform better process optimization with minimum error. The pattern produces by using analogue model can be used as the guide to develop a better computational method that captures the actual process interactions.

In terms of analogue model, further trial will be carried out for different tool features which create a novel knowledge in the field that provide the actual effect of the process.

REFERENCES

[1] M.K. Sued and D.J. Pons, "Dynamic interaction between machine, tool, and substrate in Bobbin friction stir welding," *International Journal of Manufacturing Engineering,* vol. 2016, p. 14, 2016.

[2] F.C. Liu and T.W. Nelson, "In-situ grain structure and texture evolution during friction stir welding of austenite stainless steel," *Materials & Design,* vol. 115, pp. 467-478, 2017.

[3] Y. Xiao, H. Zhan, Y. Gu, and Q. Li, "Modeling heat transfer during friction stir welding using a meshless particle method," *International Journal of Heat and Mass Transfer,* vol. 104, pp. 288-300, 2017.

[4] M. Grujicic, G. Arakere, H.V. Yalavarthy, T. He, C.F. Yen and B.A. Cheeseman, "Modeling of AA5083 material-microstructure evolution during butt friction-stir welding," *Journal of Materials Engineering and Performance,* vol. 19, pp. 672-684, 2010.

[5] Y. Zhu, G. Chen, Q. Chen, G. Zhang and Q. Shi, "Simulation of material plastic flow driven by non-uniform friction force during friction stir welding and related defect prediction," *Materials & Design,* vol. 108, pp. 400-410, 2016.

[6] M.K. Sued, D. Pons, J. Lavroff and E.H. Wong, "Design features for bobbin friction stir welding tools: Development of a conceptual model linking the underlying physics to the production process," *Materials & Design,* vol. 54, pp. 632-643, 2014.

[7] K.C.D. Sudarshan, A. Tamadon, D. Pons, M.K. Sued, D. Clucas and E.H. Wong, "Preparation of plasticine material for analogue modelling," in *Proceedings of International Conference on Design and Manufacturing*, Auckland, New Zealand, 2016.

[8] J.C. McClure, E. Coronado, S. Aloor, B.M. Nowak, L.E. Murr and A.C. Nunes, "Effect of pin tool shape on metal flow during friction stir welding," *Trends in Welding Research, Proceedings,* pp. 257-261, 2003.

Design and development of bulletproof vest using kenaf fibre embedded with X-ray films

A.M.R. Azmi[1,2,*], M.T.H. Sultan[1,2], A. Hamdan[1,2]

[1)] Aerospace Manufacturing Research Centre, Universiti Putra Malaysia, 43400 UPM Serdang, Selangor, Malaysia
[2)] Department of Aerospace Engineering, Faculty of Engineering, Universiti Putra Malaysia, 43400 UPM Serdang, Selangor, Malaysia

[*]Corresponding e-mail: mussrayney@gmail.com

Keywords: X-ray; kenaf; tensile test

ABSTRACT – Existing bulletproof vests are either too heavy, or too expensive. Therefore, a more effective performance, user friendly, lighter and cheaper bulletproof vest is desired. This study discusses tensile characterization and high velocity impact testing on new materials to replace the existing insert plate for the current available bulletproof vest. The materials chosen for this research are a natural fibre, namely kenaf and x-ray film. The materials were fabricated using the traditional hand lay-up method. From the tensile characteristics, the third configuration was proposed as the best configuration.

1. INTRODUCTION

The purpose of ballistic material is not just to stop the speeding bullets but to protect the individual from fragmenting devices such as grenades, mortars, and artillery shells as well. Ballistic resistant materials such as bulletproof vests and helmets are known to contain high strength fibres. Fibres conventionally used include aramid fibres, polyethylene (UHMWPE), nylon fibres, and glass fibres as found in previous study [1-4]. For many applications, such as vests or parts of vests, the fibres are used in a woven or knitted fabric. Sometimes, the fibres are encapsulated or embedded in a composite material.

The awareness in natural fiber application gained serious attention. The researches on natural fiber have been broader not only for ballistic but other application as well as shown in previous study [5,6]. Promoting the green composite concept, x-ray waste and biocomposite fiber reinforced are employed in this research. Lee et al. [3] found that impregnating shear thickening fluid (STF) into fabric helps enhancing the ballistic properties of the fabric significantly due to better absorbent capability. Da Luz [2] found that an epoxy composite reinforced with jute fabric can compete with Kevlar in terms of ballistic performance. By comparing the degree of energy absorption, Wambua et al. [1] found that hybrid structures have a clear advantage over mild steel and plain flax, hemp and jute composites. In addition, natural fibre is considerably lower in cost and weight and there is also the environmental and societal benefits from natural fibre as shown in previous study [6].

Hence, it gives a strong credit for the replacement of natural fibre composite as compared to existing materials.

2. METHODOLOGY

Materials chosen as the test specimens are kenaf fibre reinforced polymeric composite and x-ray films. The specimens were fabricated using traditional hand lay-up method, into four different configurations with seven layers as shown in Table 1.

Table 1 Four configurations and respective thickness.

Configuration	Layers	Thickness
1	K-X-K-X-K-X-K	6.35mm
2	K-K-X-X-X-K-K	6.40mm
3	X-X-X-X-X-X-X	1.60mm
4	K-K-K-K-K-K-K	8.15mm

K - Kenaf
X - X-ray Film

The specimens were cut based on ASTM D-3039 standard, which is 250mm x 25mm for the tensile test. The specimens were tested using Instron 3366 except for configuration 4 which was tested using Instron 3382 due to its thickness. Speed used is 1mm/min. The best configuration from tensile testing was selected and enhanced for ballistic test. The fabrication process was then improved by making it into fourteen layers of x-ray films, and sandwiching it between a layer of kenaf fibre each at the top and bottom layer. The specimens were then cut based on National Institute of Justice (NIJ) ballistic test standards which is 100mm x 100mm. They were subjected to high velocity impact test using a single stage gas gun that is calibrated using pressure which ranges the bullet velocity. Three type of bullets were used which were blunt bullets, hemispherical bullets and chisel-pointed or conical bullets. Each bullet type is tested with different pressure values naming 2 bar, 3 bar, 4 bar and 5 bar which gives different ranges of velocities.

3. RESULTS AND DISCUSSION

Figure 1 shows that configuration 3 is much more elastic compared to the other three configurations. In fact, the tensile strain for configuration 3 is at 15.29% as shown in Table 2 which is approximately seven times more than the others.

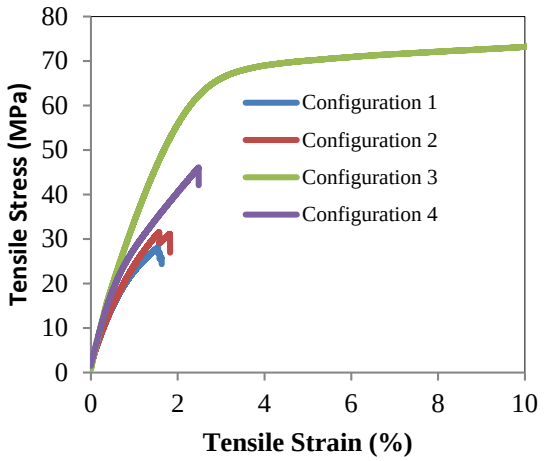

Figure 1 Tensile stress against tensile strain curve.

Table 2 Mean tensile test results.

Conf.	UTS (MPa)	Tensile Modulus (GPa)	Tensile Strain (%)
1	30.59	2.98	1.88%
2	34.15	3.05	1.84%
3	75.52	2.40	15.29%
4	49.61	3.43	2.79%

Table 2 also reports that configuration 4 which is fully kenaf shows better properties compared to configuration 1 and 2 which are hybrids. This is because the interface adhesion between kenaf and x-ray film layers in configuration 1 and 2 is very weak. Hence, it causes the kenaf to delaminate and break faster and easier.

Table 3 High velocity impact test results.

Pressure	Blunt	Conical	Hemispherical
2 bar	B	B	P
3 bar	B	B	P
4 bar	B	P	P
5 bar	P	P	P

B - Bounced
P – Penetrated

The specimens were easier penetrated by conical type bullets, followed by hemispherical type and lastly the blunt type. This is most probably because of the surface of the bullets. Most of the bullets bounced back due to the x-ray films, since the kenaf fibre layer would simply break or get chipped off after impact.

4. CONCLUSION

The layering configuration affects the tensile strength greatly. In this experiment, only four types of configurations were tried out. The two different materials do not stick well to each other using the epoxy resin. This is clearly shown during the tensile test as the hybrid specimens delaminates easily where these two materials are in contact. This might be due to the untreated kenaf fibre has a different type of surface compared to the x-ray films and makes it not react well with the epoxy resin. The main contributing material for this research are the x-ray films. The natural fibre chosen, which is kenaf fibre is not really impact resistant. This is proven from the high velocity impact test; we can see that the kenaf fibre layer does not really contribute much in absorbing energy from the bullet since it just breaks or chips off.

ACKNOWLEDGEMENT

This work was supported by UPM. The authors would like to express their gratitude and sincere appreciation to the Aerospace Engineering Department and Aerospace Manufacturing Research Centre of the Universiti Putra Malaysia.

REFERENCES

[1] P. Wambua, B. Vangrimde, S. Lomov and I. Verpoest, “The response of natural fibre composites to ballistic impact by fragment simulating projectiles,” *Compos. Struct.*, vol. 77, no. 2, pp. 232–240, 2007.

[2] F.S. da Luz, E.P. Lima Junior, L.H.L. Louro and S. N. Monteiro, “Ballistic test of multilayered armor with intermediate epoxy composite reinforced with jute fabric,” *Mater. Res.*, vol. 18, pp. 170–177, 2015.

[3] Y.S. Lee, E.D. Wetzel and N.J. wagner, “the ballistic impact characteristics of kevlar woven fabrics impregnated with a colloidal shear thickening fluid,” *Mater. Sci.*, vol. 38, p. 9, 2003.

[4] S.D. Salman, Z. Leman, M.T.H. Sultan, M.R. Ishak and F. Cardona, “Ballistic impact resistance of plain woven kenaf/aramid reinforced polyvinyl butyral laminated hybrid composite,” *BioResources*, vol. 11, no. 3, pp. 7282–7295, 2016.

[5] A. Hamdan, F. Mustapha, K.A. Ahmad, A.S. Mohd Rafie, M.R. Ishak and A. E. Ismail, “The effect of customized woven and stacked layer orientation on tensile and flexural properties of woven kenaf fibre reinforced epoxy composites,” *Int. J. Polym. Sci.*, vol. 2016, 2016.

[6] W.D. Brouwer, “Natural fibre composites saving weight and cost with renewable materials,” *Cent. Light. Struct. TUD-TNO*, p. 9, 2013.

Quasi static and dynamic perforation of PET-based sandwich structures subjected to normal and oblique angles

S.H.S.M. Fadzullah[1, 2*], O. Ifayefunmi[3], Z. Mustafa[4], G. Omar[1,2], A.H. Nurfaizey[1,2]

[1)] Faculty of Mechanical Engineering, Universiti Teknikal Malaysia Melaka, Hang Tuah Jaya, 76100 Durian Tunggal, Melaka, Malaysia.
[2)] Centre for Advanced Research on Energy, Universiti Teknikal Malaysia Melaka, Hang Tuah Jaya, 76100 Durian Tunggal, Melaka, Malaysia.
[3)] Faculty of Engineering Technology, Universiti Teknikal Malaysia Melaka, Hang Tuah Jaya, 76100 Durian Tunggal, Melaka, Malaysia.
[4)] Faculty of Manufacturing Engineering, Universiti Teknikal Malaysia Melaka, Hang Tuah Jaya, 76100 Durian Tunggal, Melaka, Malaysia.

[*]Corresponding e-mail: hajar@utem.edu.my

Keywords: Low velocity impact; oblique; quasi-static; perforation; composite structures

ABSTRACT – To-date, very few research has reported on the perforation behaviour of sandwich structures when subjected to varying inclination angles, at quasi-static and dynamic loading rates. Hence, this research aims to investigate the perforation behaviour of polymeric foam cored sandwich structures when subjected to quasi-static and dynamic loading at 0°,10° and 20° inclination angles. Here, a crosshead displacement rate of 1 mm/min and impact velocity at 3.78 ms^{-1} was considered for the quasi-static and dynamic loading, respectively. The dynamic load required to cause a given deflection is higher than those of the quasi-static conditions, due to (i) enhanced strength and stiffness of the components due strain rate effects and (ii) inertia effect. Furthermore, it is the normal impact (0°) that results in the highest peak force, for both quasi-static and dynamic test conditions. Knowledge in this area will aid in prediction of failure behaviour and damage prediction for such materials.

1. INTRODUCTION

Impact events can occur during the manufacturing process, in-service operation as well as during the life of a structure or component. In addition, it should be noted that most impact events are non-normal or oblique in nature [1]. Moreover, limited work has focused on the oblique impact response of composites and sandwich structures Most of these works are dedicated to ballistic impact [1-2].

Three important steps of panel failure during deformation in a sandwich structure; (i) initial failure where one of the skins of the panel is fractured, with or without considerable deformation of the core; (ii) penetration of the indenter through the thickness of the panel; and (iii) perforation of the panel when the whole of the indenter has emerged through the panel.

More recently, Zhou et al., [3] predicted the perforation resistance of the sandwich panels when subjected to oblique impact. For a given type of sandwich panel, the normal impact exhibits the highest maximum impact force. The corresponding perforation energy was found to increase with impact angle. In addition, further investigation was made on the damage evolution, with the focus on the perforated panels made with cross-linked PVC sandwich composites and PET sandwich composites subjected to oblique impact at incident angles of 0°, 10°, 20° and 30°, respectively.

This paper aims to examine the effect of different loading conditions on the perforation behavior of PET foam cored sandwich structures when subjected to both quasi-static indentation test and drop-weight impact at energies up to 40 J with inclination angles of 0º,10° and 20º.

2. METHODOLOGY

2.1 Fabrication of the sandwich structures

The top and bottom skins of the sandwich structures were manufactured using four plies of glass fiber reinforced epoxy, with a stacking sequence of [0/90]s, and 1.0 mm thick. The laminates were then placed on either side of the PET foam core (AIREX® T92.130, UK). The skin material is of unidirectional E-glass fiber reinforced epoxy resin, with nominal ply thickness of 0.25 mm (SE84, UK). The nominal density of PET foam core is 135 kg/m^3 and thickness of approximately 20 mm each. The sandwich was assembled between two steel plates and cured under a pressure of 1.25 bars in a hot press at 80° ± 5°C for a dwell time of 90 minutes before slow cooling to room temperature. The final cured dimensions of the sandwich structures are 150 mm (L) x 150 mm (W) with cured thickness of 20 mm.

2.2 Indentation test

A series of indentation tests were carried out using an Instron 4505 test machine at a crosshead displacement rate of 1 mm/minutes. The test samples were centrally loaded and fully clamped using a 100 mm-diameter circular steel ring, in which the test samples. For tests at inclined angles, a customized jig was used.

2.3 Impact perforation of the sandwich structures

The impact response of the sandwich structures was assessed using an instrumented drop-weight impact rig. Here, a 5.6 kg-carriage of impact mass, with a 12-mm diameter steel hemispherical indenter was used to strike impact energies up to 40 J, at normal (0°) and oblique angles of 10° and 20°. The impact velocity measured was at approximately up to 3.78 m/s. Similar boundary conditions as used in the indentation test was set for the series of test under this loading rate.

3. RESULTS AND DISCUSSION

Typical load-time traces following quasi-static indentation and drop-weight impact test at 0°, 10° and 20° angles are given in Figures 1(a) to (c). Clearly, the dynamic loading exhibit much higher force magnitude in comparison to the quasi-static indentation response, as tabulated in Table 1, with the ratio of 1.4, 1.8 and 1.9 for the 1st peak force against the quasi-static ones at inclination angles of 0°,10° and 20°.Meanwhile, the second peak force values reflect much higher ratio between the dynamic and the quasi-static data with the values of 2.0, 1.4 and 1.2 for inclination angles of 0°, 10° and 20°. These findings are in agreement with the numerical work by Zhou et al. [3], due the strain rate sensitivity of the glass fiber reinforced epoxy skins (velocity speed of 3.78 m/s against 1 mm/min) as well as the effect of inertia, with an increase in inclination angle from 0° to 20° [4]. From Fig 1(a), for θ=0°, the first peak force captured, which is associated with failure or fracture of the top skin is higher than the second peak force (failure of the lower skin) for the quasi-static case. Observations from the results at θ=10° revealed that a similar observation is found for the results from both the quasi-static and dynamic loading conditions. At higher inclination angle (θ=20°), a similar trend to the θ=10° cases following quasi-static loading is observed. Interestingly, the valley between the two peaks, which is associated with perforation of the foam, indicates that quasi-static loading yields a higher value. This may be due to greater amounts of damage suffered in the sandwich panels subjected to impact loading, particularly in terms of the failure of the core at this impact energy, leading to significant strength and stiffness reduction.

4. CONCLUSIONS

Overall, it can be concluded that regardless of whether the test was conducted at normal or other inclination angles, the dynamic load required to cause a given deflection is higher than those of the quasi-static conditions, mainly due to enhanced strength and stiffness of the components due to rate-dependent material properties and secondly inertia effect. In addition, it is the normal impact that results in the highest peak force. In addition, both the first and the second peak force reduced with increasing inclination angle, in passing from 0° to 20°. However, the average force, which corresponds to densification of the foam core shows an increase with inclination angle. Understanding of the material response when subjected both loading conditions (or strain rate) at varying inclination angles will aid in prediction of failure behaviour and damage prediction for such materials.

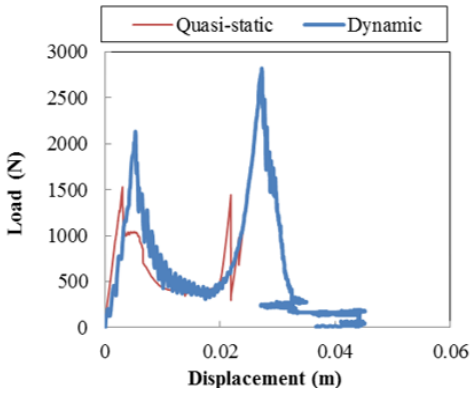

(a)

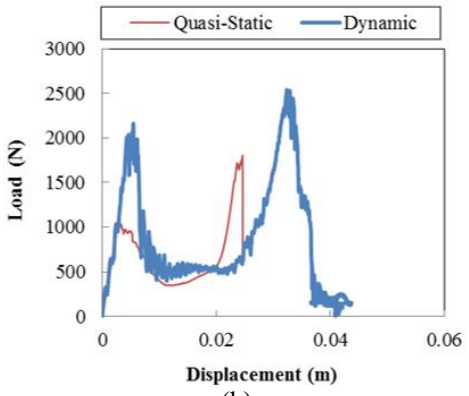

(b)

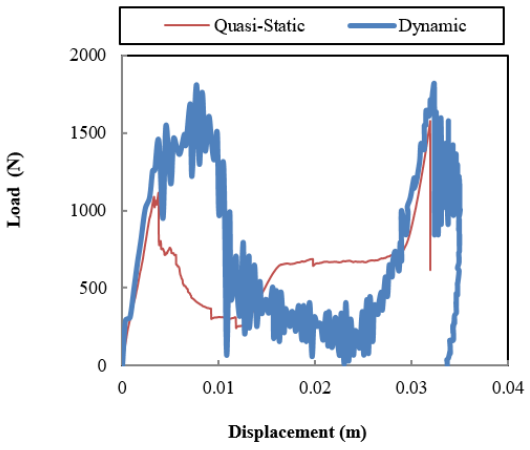

(c)

Figure 1 Typical load-time traces on the PET (T92.130) sandwich structures subjected to inclination angles of (a) θ= 0°; (b) θ= 10° and in (c) θ= 20°.

Table 1 Experimental results following dynamic and quasi static loading on the PET sandwich structures at normal and inclined (oblique) angles.

Type of test	Inclination angle (°)	1st Peak (N)	2nd Peak (N)	Average Force (N)
Quasi-Static Indentation	0	1530 ± 31	1443± 50	408± 12
	10	1192 ± 30	1805± 62	414± 21
	20	1112± 24	1573± 67	523± 18
Dynamic (low velocity impact)	0	2133 ± 107	2821 ± 127	481 ±10
	10	2162 ± 112	2540 ± 135	457 ±18
	20	2065 ± 74	1890 ± 87	314 ± 8

REFERENCES

[1] S. Abrate, Impact on composite structures. Cambridge University Press, 2005.

[2] S. Madjidi, W.S. Arnold and I.H. Marshall, "Damage tolerance of CSM laminates subject to low velocity oblique impacts," *Composite Structures*, vol. 34, no. 1, pp. 101–116, 1996.

[3] M.Z. Hassan and W.J. Cantwell, "The influence of core properties on the perforation resistance of sandwich structures – an experimental study," *Composites Part B: Engineering*, vol. 43, no. 8, pp. 3231–3238, 2012.

[4] J. Zhou, M.Z. Hassan, Z. Guan and W. J. Cantwell, "The low velocity impact response of foam-based sandwich panels," *Composites Science and Technology*, vol. 72, no. 14, pp. 1781–1790, 2012.

Effect of annealing temperature towards electrical properties of indium zinc oxide modified kenaf fibre through dip-coating method

O. Edynoor[1,2,3], T. Moriga[1,2*], K. Murai[1], A.R.M. Warikh[2,3]

[1)] Department of Chemical Science and Technology, Graduate School of Advanced Technology and Science, Tokushima University, 2-1 Minami-Josanjima, 770-8506 Tokushima, Japan
[2)] Tokushima-UTeM Academic Center, Tokushima University, 2-1 Minami-Josanjima, 770-8506 Tokushima, Japan
[3)] Faculty of Manufacturing Engineering, Universiti Teknikal Malaysia Melaka, Hang Tuah Jaya, 76100 Durian Tunggal, Melaka, Malaysia

*Corresponding e-mail: moriga@tokushima-u.ac.jp

Keywords: Electrical; indium zinc oxide; kenaf

ABSTRACT – This study illustrates the effect of annealing temperature towards Indium Zinc Oxide (IZO) modified Kenaf Fibre (KF). IZO was successfully added onto KF by a dip-coating method. The electrical conductivity of Indium Zinc Oxide modified Kenaf Fibre (KF-IZO) was investigated and as indicated by a transformation in its morphology and annealed temperature. As a result, 150ºC annealed temperature was presented as the highest value of electrical conductivity, 11.81 S/mm and the lowest KF loss weight is 4.27%. Scanning Electron Microscope/Energy Dispersive Using X-ray (SEM/EDX) analysis revealed that the IZO film was uniformly coated with the KF substrates, and no significant thermal damage was observed.

1. INTRODUCTION

Recently, natural fibres play a vital role in the sustainable development, especially amongst manufacturing industries. Thus, natural fibres namely Kenaf, jute, sisal, hemp and bamboo are utilized and are sought for their potential within the manufacturing industry. With respect to KF, it offers low cost and low density materials with good mechanical properties and recyclability [1]. Hydrophilic quality of fibres is a major problem for most natural fibres. As a previous study [2] suggests, natural fibres need to be treated to make them compatible with hydrophobic material. Additionally, most natural fibres have low degradation temperatures (~200ºC), which make them incompatible with the high curing temperatures on any process that involves high temperatures [3].

In this study, transparent coating oxide-indium zinc oxide (TCO-IZO) modified KF enhances the usability of KF itself. For instance, TCO-IZO which was ZnO as precursor and Indium as a dopant material are successfully used as conductive materials and applied at various industries as electronics and semiconductors. Earlier, glass, sapphire and polymer materials were substrates used for TCO-IZO. Whereas, this study will be focusing on KF as the main medium to carry IZO as a conductive material. Even though Indium has been selected as a dopant material, due to high costs and scarcity, it has low usability. [4]. Smart textile, composite technology (EMI shielding), bio electronic electromagnetic and electrostatic discharge (ESD) protective is applicable to areas where KF with TCO-IZO could be applied.

2. METHODOLOGY

Initially, KF (800GSM) in the form of a randomly oriented mat was supplied by Innovative Pultrusion Sdn. Bhd. KF was alkalized by using Sodium Hydroxide (NaOH) solution with 5% concentration and immersed for 48 hours at room temperature. It was rinsed accordingly for 5 times with deionized water and continued to be dried at 80ºC for 24 hours in a vacuum furnace. Meanwhile, IZO solution was prepared by using 9g of Zinc Acetate Dihydrate, dissolved in 300ml of ethanol (precursor) at room temperature (25ºC) and magnetically stirred for about 1 hour. During the process, deionized water (~ 8ml) as stabilizer was dropped with a syringe. After complete dissolution, the solution was continuously mixed with 0.81g of Indium (III) Chloride (doping) for 1 hour at 75ºC. This resulted in a clear yield and a homogenous solution of IZO is obtained.

The dip-coating process was applied to KF at room temperature of 27ºC. KF was added t- IZO by dip coating machine at a 5mm/sec dipping rate. After being deposited, KF-IZO continues to be dried at 120ºC and followed by an annealing process at 150 ºC, 175 ºC and 200ºC for 4 hours in vacuum furnace. Additionally, a focused ion beam (JEOL (JEM-9320FIB)) was used to cut the KF cross-section, which was then scanned by SEM/EDX (JEOL (JSM-6510A) for qualitative measurements. Electrical measurements test, through the four probe method (Hewlett Packard 34401A multi-meter with Advantest R6144 voltmeter) along with a copper attachment, acted as the line contact between the adjacent fibres along the KF-IZO surface area.

3. RESULTS AND ANALYSIS

As referred to Figure 1 (a) and (b), Zinc (Zn) elements clearly existed around KF. It depicts that IZO was successfully coated with KF and the qualitative scanning image also proves that Zinc, distinctive through a pink colour, was homogenously distributed. This can be termed as favourable electrical properties of KF-IZO.

Low annealing temperatures are strictly required for natural fibres, owing to its applicability in low

temperatures alone. Thermogravimetric analysis (TGA) result shows that KF strongly decomposed at 219.25ºC with about 88.17% of remaining KF weight (Figure 2). In a prior study [5], it was claimed that KF must be operated in low processing temperatures (≤200ºC). Table 1 shows parallel results, where KF loss weight increased with an increase in annealed temperature.

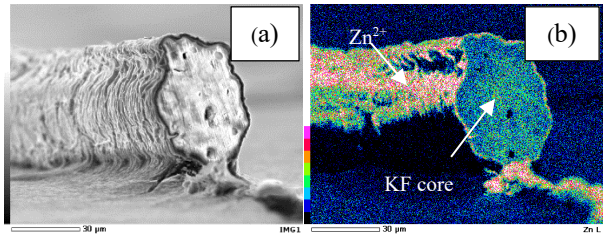

Figure 1 (a) KF-IZO SEM images (b) KF-IZO scanned for detection Zn element (pink colour).

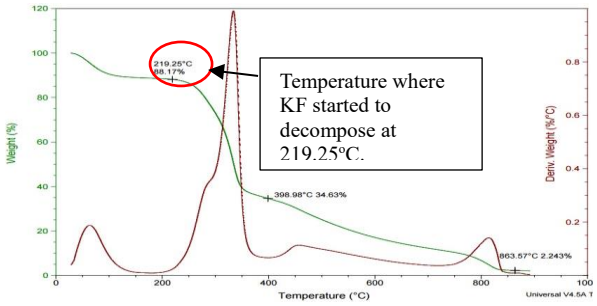

Figure 2 TGA result for kenaf fibre (KF).

Table 1: KF loss weight dependence annealed temperature.

Annealed Temp (ºC)	Loss weight of KF (%)
150	4.27
175	8.92
200	10.95

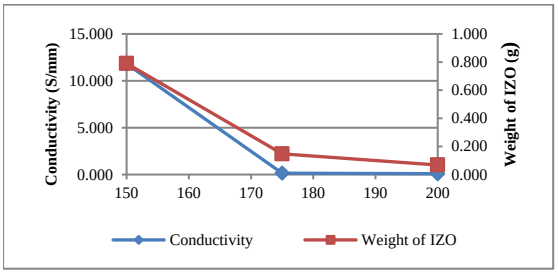

Figure 3 Dependence of temperature on conductivity.

KF decomposition result indicates that at temperatures ranging from 150 ºC to 200ºC, KF lost about 4% - 11% in a total weight (as represented in Table 1). This creates an obstacle towards electrical current conduction of KF-IZO, as illustrated in Figure 2. As the temperature increased, the amount of oxygen desorption increased, and free carriers in the thin films also increased [6]. It was observed that with the increase of the annealing temperature of IZO (In_2O_3: ZnO = 90:10 wt.%) from 100ºC – 300ºC, the carrier concentration decreased and the resistivity increased. With a rise in annealed temperatures, the amount of KF weight lost increased, resulting in build-up of carbon concentration on KF substrates, as reported in Table 1. The existing large amount of carbon created a barrier towards IZO coating in order to conduct electrical charges. Carbon is known as a non-metallic material and a good conductor with low electrical conductivity. Also, carbon residue can be seen on the samples as seen in the colour change in KF-IZO due to annealing temperature (Figure 3). It shows that at 200ºC annealed temperature, KF-IZO turns blackish in colour and KF seems burnt and decomposed when compared to the 150ºC samples. In addition, the reaction between IZO layers towards the KF surfaces during the annealing process caused another catastrophic change on KF structure and made it more brittle.

150ºC **175ºC** **200ºC**

Figure 4 KF-IZO appearance after annealed process; 150 ºC, 175 ºC and 200ºC (MORITEX – Scopemen series with 166x magnification).

4. CONCLUSION

The potential of KF as an electrical conductor was discovered with an emphasis on surface morphology and its annealed temperature effect towards electrical conductivity. The highest electrical conductivity of 11.81 S/mm was achieved at 150ºC with KF loss weight 4.27%. The SEM-EDX results revealed that Zn element existed on KF substrates and were uniformly distributed.

REFERENCES

[1] B.V.R Raman, R.B Vijay and N. Manoharan, "Kenaf fibre resin reinforced composites: A review," *ARPN J. Eng. and Appl. Sci.*, vol. 10, no. 13, pp. 5483-5484, 2015.

[2] H. Aziz Sharifah, P. Ansell Martin, J. Simon, R. Clarke and Panteny, "Modified polyester resins for natural fibre composites," *Compos. Sci. and Technol.*, 65, pp.525-535, 2005.

[3] N. Sgriccia, M.C. Hawley and M.Misra, 2008.Characterization of natural fiber surfaces and natural fiber composites. *Compos.: Part A*, vol. 39 pp. 1632–1637, 2008.

[4] K. Ellmer, "Past achievements and future challenges in the development of optically transparent electrodes," *Nat. Photonics*, vol. 6 no. 12 pp 809-817, 2012.

[5] B. Wielage, T. Lampke, G. Marx, K. Nestler and D. Starke, "Thermogravimetric and differential scanning calorimetric analysis of natural fibers and polypropylene," *Thermochim. Acta*, 337(169), 1999.

[6] S-H Lee, S-Y Lee and B-O Park, "Effect of annealing temperature on amorphous indium zinc oxide thin films prepared by a sol-gel spin-coating method," *J. Korean Cryst. Growth and Cryst. Technol.*, vol. 22, no. 1, pp 15-18, 2012.

The influence of electrospinning distances on fibre diameter of poly(vinyl alcohol) electrospun nanofibres

F.C. Long[1], R.A. Kamsom[1], A.H. Nurfaizey[1,2,*], M.H.M. Isa[1,2], N.A.B. Masripan[1,2]

[1)] Faculty of Mechanical Engineering, Universiti Teknikal Malaysia Melaka, Hang Tuah Jaya, 76100 Durian Tunggal, Melaka, Malaysia
[2)] Centre for Advanced Research on Energy, Universiti Teknikal Malaysia Melaka, Hang Tuah Jaya, 76100 Durian Tunggal, Melaka, Malaysia

[*]Corresponding e-mail: nurfaizey@utem.edu.my

Keywords: Electrospinning; electrospun nanofibre; electrospinning distance; fibre diameter

ABSTRACT – One of the important parameters in electrospinning process is the distance between tip and collector also known as electrospinning distance. Insufficient distance would produce fibres with various defects. This paper explores the influence of electrospinning distances on fibre diameter of poly(vinyl alcohol)(PVA) electrospun nanofibres. PVA nanofibre samples were produced at a constant applied voltage but varying electrospinning distances. The morphology of the nanofibres were observed under scanning electron microscope and ImageJ software was used to measure the fibre diameter. Knowledge gained from this study is useful for finding an optimum condition for producing defect-free fibres.

1. INTRODUCTION

Electrospinning is one of the most widely used methods for producing ultra-thin polymeric nanofibres using electric charge [1]. When an adequate electric potential is applied to a polymer solution, a straight jet of polymer is ejected from the electrospinning tip before undergoing a spiral looping motion known as the whipping instability [2]. As the fibres move towards the collector, solvent evaporation and fibre stretching continues before landing on the collector as randomly oriented fibres [1,2].

One of the crucial parameters in electrospinning is the distance between tip to collector. Insufficient distance would produce fibres with various defects such as non-uniform, thick, ribbon-shaped, or wet fibres [4]. A good electrospinning condition should have a sufficient electrospinning distance for solvent evaporation and fibre thinning to take place [4] but at the same time the distance must be close enough to maintain adequate electrical potential gradient to drive the deposition process [5]. Often, this optimum combination varies depending on other electrospinning parameters including the type of polymer being used.

This study investigates the influence of electrospinning distance on fibre diameter of PVA electrospun nanofibres. Knowing the optimum conditions for electrospinning would produce defect-free fibres suitable for its intended applications.

2. METHODOLOGY

All experimental works were carried out using Electrospinz Model ES1a (Electrospinz Ltd., NZ). Poly(vinylalcohol)(PVA) with an average molecular weight of 124,000-130,000 g/mol. The PVA was dissolved in distilled water to a final concentration of 8 wt.%. The mixture was stirred approximately for 2 hours at 60°C using a magnetic stirrer Model C-MAG HS7 (Ika Works, Malaysia). PVA nanofibre samples were produced at a constant applied voltage of 10 kV but varying electrospinning distances as listed in Table 1. The morphology of the electrospun nanofibres was observed under scanning electron microscope Model JSM-6010PLUS/LV (JEOL Ltd., Japan). The samples were sputtered with platinum for 180 seconds using JEOL JEC-300FC auto fine coater. From the SEM micrographs, the average fibre diameters were measured using ImageJ software v1.50 (National Institutes of Health, USA).

Table 1 Electrospinning samples and parameters.

Voltage (kV)	Distance (cm)	Sample
10	6	A
	8	B
	10	C
	12	D
	14	E
	16	F
	18	G
	20	H

3. RESULTS AND DISCUSSION

The scanning micrographs of the nanofibre samples are shown in Figure 1. When the tip to collector distance was set at 6 cm, wet nanofibres were produced as can be seen in Figure 1 (a). This suggests that at 6 cm, the electrospinning distance was insufficient for solvent evaporation to take place thus wet, thick, and nonuniform fibres were produced [4]. When the electrospinning distance was increased to 8 cm, solid and uniform fibres were produced as in Figure 1(b). After that, subsequent increase in electrospinning distance does not show significant difference in terms of fibre morphology. Smooth and uniform fibres were produced from electrospinning distances of 8 to 20 cm (Figure 1 (b)-(h)). From the results, it is safe to note that with electrical potential of 10 kV, electrospinning of this particular grade

of PVA would require a minimum tip to collector distance of 8 cm.

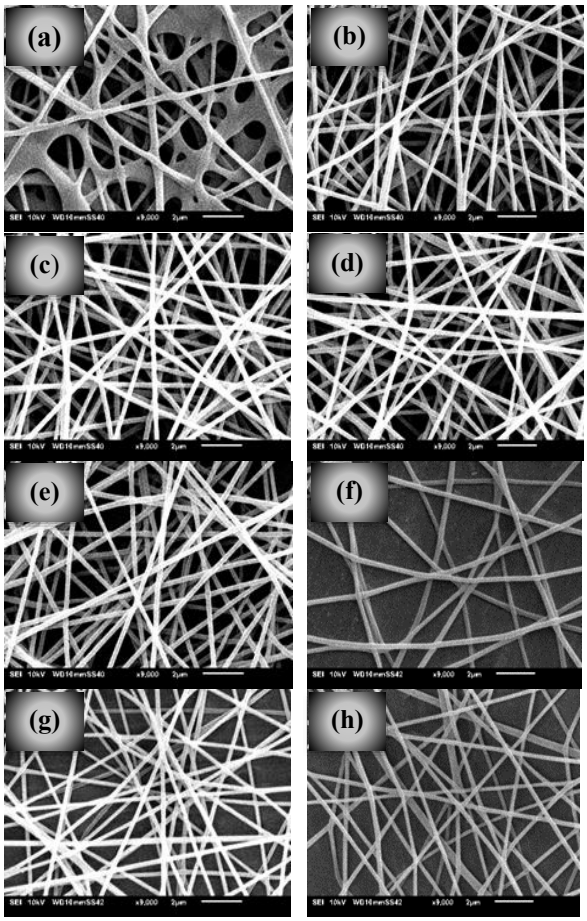

Figure 1 SEM micrographs of PVA nanofibres with different tip to collector distances (a) 6cm (b) 8cm (c) 10cm (d) 12cm (e) 14cm (f) 16cm (g) 18cm (h) 20cm.

For each of the SEM micrograph, the measurement of fibre diameter was taken at 100 locations to minimize error. The measured diameters are presented in the form of histogram as shown in Figure 2. For sample A, the diameter of the fibres were immeasurable due to the formation of wet fibres. For sample B, C, and D, a slight variation of fibre diameter between 224 to 260 nm were found with the thinnest fibres shown by sample B at electrospinning distance of 8 cm. However, this variation is less than 14% and therefore considered insignificant. The variation could be due to errors when conducting the measurement. Significant change in fibre diameter (~30%) can be seen when the electrospinning distance was increased from 14 to 20 cm. The results seem to be consistent with a previous study which concluded that the diameter of electrospun nanofibres can be reduced by extending the electrospinning distance, thus prolonging the stretching time of the fibres [6]. However, at a constant applied voltage, extending the electrospinning distance would reduce the electric field strength as it is inversely proportional to the distance [3]. This will lead to less fibre drawing and lower production rate as evident by thinner depositions of sample F, G, and H (Figure 1). Future works investigating different type of materials and parameters are ongoing and the results will be reported later.

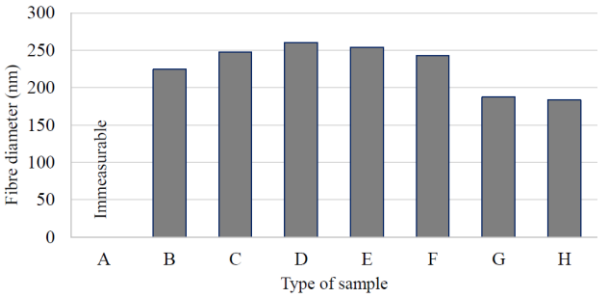

Figure 2 Average fibre diameters of the samples.

4. CONCLUSION

Electrospinning distance was found to have significant influence on morphology and fibre diameter of PVA electrospun nanofibres. At a constant applied voltage of 10 kV, a minimum of 8 cm electrospinning distance was required. Increasing the electrospinning distance would produce thinner fibres as there is more time available for solvent evaporation and fibre stretching to take place. The results from this study is useful for determining the optimum condition to produce defect-free fibres.

ACKNOWLEDGEMENT

Special thanks to the Ministry of Higher Education Malaysia and Universiti Teknikal Malaysia Melaka (UTeM) through FRGS/2/2014/TK01/FKM/02/F00233 and MyBrain15.

REFERENCES

[1] W.-E. Teo, R. Inai, and S. Ramakrishna, "Technological advances in electrospinning of nanofibers," *Sci. Technol. Adv. Mater.*, vol. 12, p. 13002, 2011.

[2] S. Agarwal, A. Greiner and J.H. Wendorff, "Functional materials by electrospinning of polymers," *Prog. Polym. Sci.*, vol. 38, no. 6, pp. 963–991, 2013.

[3] A.H. Nurfaizey, J. Stanger, N. Tucker, N. Buunk, A. R. Wood and M. P. Staiger, "Control of Spatial Deposition of Electrospun Fiber Using Electric Field Manipulation," *J. Eng. Fabr. Fibers*, vol. 9, no. 1, pp. 155–164, 2014.

[4] Z. Li and C. Wang, "Effects of Working Parameters on Electrospinning," *One-Dimensional nanostructures*, pp. 15–29, 2013.

[5] A.H.N.N. Tucker, M.P. Staiger, "Functional nanofibers in clothing for protection against chemical and biologicl hazards," in *Functional nanofibers and their application*, Woodhead Publishing Limited, pp. 236–261,2012

[6] M. Chowdhury and G. K. Stylios, "Analysis of the effect of experimental parameters on the morphology of electrospun polyethylene oxide nanofibres and on their thermal properties," *J. Text. Inst.*, vol. 103, no. November 2014, pp. 124–138, 2012.

The tensile properties characterisation on recycled polypropylene and polyethylene blend

M.J. Taufiq[1], M.R. Mansor[1,2,*], Z. Mustafa[3], M.N.A. Nordin[1,2]

[1)] Faculty of Mechanical Engineering, Universiti Teknikal Malaysia Melaka, Hang Tuah Jaya, 76100 Durian Tunggal, Melaka, Malaysia
[2)] Centre for Advanced Research on Energy, Universiti Teknikal Malaysia Melaka, Hang Tuah Jaya, 76100 Durian Tunggal, Melaka, Malaysia
[3)] Faculty of Manufacturing Engineering, Universiti Teknikal Malaysia Melaka, Hang Tuah Jaya, 76100 Durian Tunggal, Melaka, Malaysia

[*]Corresponding e-mail: muhd.ridzuan@utem.edu.my

Keywords: Recycled polymer blend; virgin polymer blend; tensile properties

ABSTRACT – This paper presents tensile characterisation on recycled polypropylene (PP) and polyethylene (PE) blend, denoted as PP/$PE_{recycle}$. The inventiveness of study is producing a PP/PE blend that sourced from unused-rejected baby diapers as supporting "waste to wealth" initiative. The recycled plastic is readily in shredded with the constituent of 70 wt.% PP and 30 wt.% PE, averagely. The aim of study is to study the tensile properties of the PP/$PE_{recycle}$ with comparison to virgin PP/PE (PP/PE_{virgin}). The tensile test was done accordance ASTM D638 by using Instron universal testing machine. The result of tensile test has shown the tensile strength for PP/$PE_{recycle}$ is 50% lower compared to PP/PE_{virgin}. In addition, results also shown that the tensile modulus for PP/$PE_{recycle}$ is 60% lower compared to PP/PE_{virgin}. In conclusion, the use of PP/$PE_{recycle}$ is can be used in low structural loading applications to suit its tensile characteristics.

1. INTRODUCTION

Nowadays, plastic has contributed significant roles in human daily life. The approaches on enhancing the plastic mechanical properties including blending of two different types of plastic have been reported. For example, the study on PP/PE blend has been done by Chiu et al [1]. The result from their study, the tensile strength of PP, PE, and PP/PE blend are 24.1, 29.3, and 34.5 MPa, respectively. The tensile strength for the PP/PE blend was 15% decreasing compared to PP, but 17% increment in comparison to PE. This proven the tensile strength of blend was balanced in between tensile strength of PP and PE. Similarly, Run Su et al [2] have reported the mechanical properties of polypropylene and linear low density polyethylene (PP/LLDPE) blend, with variation of LLDPE content, 30, 40, 50, 60, and 70%. In their results, the impact strength increased linearly as the LLDPE content increased by 10%. However, the tensile properties decreased linearly as the LLDPE content increased by 10%. Similar study also has been demonstrated by Strapasson et al [3]. The study was conducted with the blending ratio PP/LDPE, 100/0, 75/25, 50/50, 25/75, and 0/100. The increment of LDPE content has shown the increment of impact strength and changed the failure mode from brittle to ductile. This increment also has reduced the tensile strength and tensile modulus.

In contrast, the studies on recycled plastic characterizations also have been published. First, Bertin and Robin [4] carried out the comparison of virgin LDPE/PP and post-consumer LDPE/PP blends. The yield tensile strength of post-consumer LDPE/PP was 7% higher compared to virgin LDPE/PP. Second, the using of post-consumer plastic as wood-plastic-composite matrix has been studied by Turku et al. In their study, the post-consumer plastics were blended with virgin LDPE, and wood floor was used as filler. The post-consumer plastics were resourced from municipal plastic waste and construction plastic waste. Third, the comparison study on mechanical properties between virgin and recycle HDPE as the biocomposite matrix has been done by Adhikary et al [5]. The recycle HDPE is obtained from local plastic recycling plant. From their study, the tensile strength of recycle HDPE is 23.2 MPa, which is 8% higher compared to virgin HDPE.

From the same motivation, the aim of this paper is to study the tensile properties by performing the tensile test on PP/$PE_{recycle}$ blend that obtained from recycled material. To keep minimum sample preparation cost, there is no compatibilizer was used during sample preparation. The results of PP/$PE_{recycle}$ later been compared to PP/PE_{virgin}, which prepared by same methods.

2. METHODOLOGY

2.1 Sample preparation

The recycled PP/PE from unused-rejected baby diapers with constituent of 70% PP and 30% PE was obtained from ZFH Industries Sdn. Bhd (Klang, Malaysia). The virgin PP and LLDPE were obtained from Lotte Chemical Titan and Polyethylene Malaysia respectively. The materials were compounded by using twin rotor with opposing rotating axis internal mixer (ThermoFisher) at set temperature = 200°C (± 7°C). After that, the compounded materials were crushed using crusher machine (TW-SC-400F) and later moulded using laboratory hot press moulding (GoTech). The materials were pressed under 20 tons for 15 minutes at 200 ± 2°C.

2.2 Tensile testing

Five tensile samples were cut from moulded plate. The tensile test samples were prepared accordance to ASTM D638 [6] and tested on universal testing machine (Instron) with speed of testing = 2mm/min, crosshead speed = 0.1 mm/min, and load capacity 25kN. An extensometer was used for detecting the elongation on the sample during test.

3. RESULTS AND DISCUSSION

Figure 1 and 2 represent the comparison of tensile properties between PP/$PE_{recycle}$ and PP/PE_{virgin} blends. The PP/$PE_{recycle}$ has reduced in yield strength (8.3 ± 0.4 MPa) compared to PP/PE_{virgin} (16.9 ± 1.5 MPa) which indicates the recycled plastic has lower stiffness. Furthermore, PP/$PE_{recycle}$ showed 60% lower in tensile modulus compared to PP/PE_{virgin}, 250 ± 34 MPa and 683 ± 54 MPa respectively. Based on both situations, the behaviour of recycled blend probably due to more deterioration of the polymer chains compared to virgin blend [7]. In addition, the tensile properties of PP/$PE_{recycle}$ might be caused by impurities that came with the recycled material. These impurities could affect the mechanical properties of PP/$PE_{recycle}$ blend as mentioned by Adhikary et al. [5].

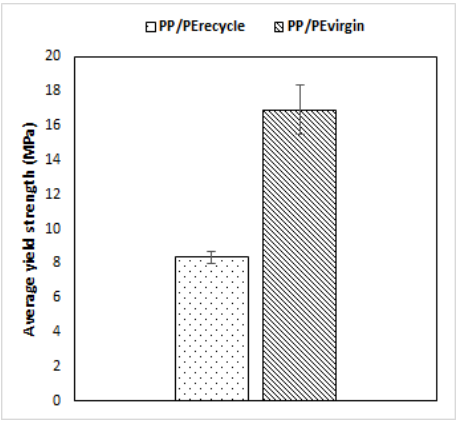

Figure 1 Average yield strength of two type of PP/PE blends.

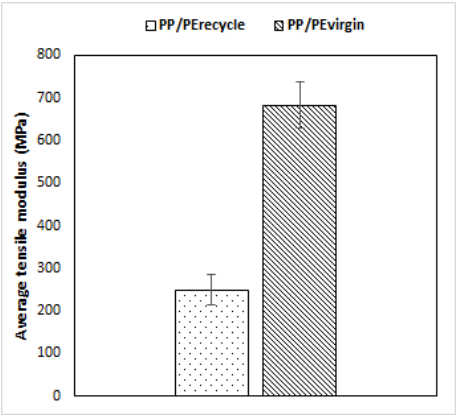

Figure 2 Average tensile modulus of two type of PP/PE blends.

4. CONCLUSION

As conclusion, the tensile characterisations of PP/$PE_{recycle}$ has been done with comparison to PP/PE_{virgin}. The characterisations also done with both samples were prepared without using additive. In comparison to PP/PE_{virgin}, PP/$PE_{recycle}$ has low in both average yield strength by 50 ± 1 % and average tensile modulus by 60 ± 1%. Even though PP/$PE_{recycle}$ blend has lower tensile properties, however it may reduce the raw material cost and towards "waste to wealth" initiative. The next study will be the study on effect of kenaf fibre loadings on PP/$PE_{recycle}$ mechanical properties.

ACKNOWLEDGEMENT

The authors acknowledge with thanks to the fund and support from the Universiti Teknikal Malaysia Melaka (PJP/2015/FKM(3A)/S01409) and ZFH Industries Sdn Bhd on the raw materials.

REFERENCES

[1] F.C. Chiu, H.Z. Yen and C.E. Lee, "Characterization of PP/HDPE blend-based nanocomposites using different maleated polyolefins as compatibilizers," *Polym. Test.*, vol. 29, no. 3, pp. 397–406, 2010.

[2] R. Su, K. Wang, Q. Zhang, F. Chen and Q. Fu, "Effect of melt temperature on the phase morphology, thermal behavior and mechanical properties of injection-molded PP/LLDPE blends," *Chinese J. Polym. Sci.*, vol. 28, no. 2, pp. 249–255, 2010.

[3] R. Strapasson, S.C. Amico, MF.R. Pereira and T.H.D. Sydenstricker, "Tensile and impact behavior of polypropylene/low density polyethylene blends," *Polym. Test.*, vol. 24, no. 4, pp. 468–473, 2005.

[4] S. Bertin and J.J. Robin, "Study and characterization of virgin and recycled LDPE/PP blends," *Eur. Polym. J.*, vol. 38, no. 11, pp. 2255–2264, 2002.

[5] K.B. Adhikary, S. Pang and M.P. Staiger, "Dimensional stability and mechanical behaviour of wood-plastic composites based on recycled and virgin high-density polyethylene (HDPE)," *Compos. Part B Eng.*, vol. 39, no. 5, pp. 807–815, 2008.

[6] *ASTM D638 -14: Standard Test Method for Tensile Properties of Plastics*, vol. 14. West Conshohocken: ASTM International, 2004.

[7] M.M. Raj, H.V. Patel, L.M. Raj and N.K. Patel, "Studies on mechanical properties of recycled polypropylene blended with virgin polypropylene," *Int. J. Sci. Inven. Today*, vol. 2, no. 3, pp. 194–203, 2013.